Conformational dynamics of a nicotinic receptor neurotransmitter binding site

Mrityunjay Singh[1], Dinesh C. Indurthi[2], Lovika Mittal[1], Anthony Auerbach[2], and Shailendra Asthana[1].

[1]Computational Biophysics and CADD Group, Computational and Mathematical Biology Center, Translational Health Science and Technology Institute, NCR Biotech Science Cluster, Faridabad 121001, India.

[2]Department of Physiology and Biophysics, University at Buffalo, State University of New York, Buffalo, United States.

Corresponding Authors

Shailendra Asthana: sasthana@thsti.res.in

Anthony Auerbach: Anthony.auerbach@gmail.com

Dinesh C. Indurthi: dinesh.indurthi@gmail.com

Key words: acetylcholine, allostery, agonist, molecular dynamics, ion channel

Abstract

Agonists turn on receptors because they provide net favorable binding energy to active versus resting conformations of their target sites. We used simulations to explore conformational dynamics of the weak→strong binding transition at the *Torpedo* α–δ nicotinic acetylcholine receptor orthosteric site. Using 4 agonists, the alternative site conformations were identified in trajectories generated from a single starting structure by matching binding energies calculated *in silico* with those measured experimentally *in vitro*. The weak→strong transition starts with a rotation of the agonist about its cationic center ('flip'), followed by a downward displacement of loop C that repositions αY190 ('flop'), followed by formation of H-bonds between the ligand, a structural water and the δ subunit loop E backbone ('fix'). The result is a compact, hydrophobic and stable pocket with higher affinity for agonists. The simulations reveal a transient intermediate state in the weak→strong transition.

Introduction

Adult vertebrate skeletal muscle nicotinic acetylcholine receptors (AChRs) are allosteric proteins that mediate synaptic transmission between motor neurons and muscle fibers. These pentameric ligand-gated ion channels are composed of four different subunits (2 α1, β1, δ, and ε) arranged symmetrically around a central ion-conducting pore (Rahman et al., 2020; Unwin, 1993). Binding of the neurotransmitter acetylcholine (ACh) or other agonists to two orthosteric sites in the extracellular domain (ECD) increases the probability of a global change in protein 3D conformation that activates a distant (~60.0 Å) allosteric site (a gate) in the transmembrane domain (TMD), allowing cations to cross the membrane.

At the start of the channel-opening isomerization the neurotransmitter sites switch from having a low to a high affinity for agonists (LA→HA), and at the end the gate switches from closed to open (C→O) (Grosman et al., 2000; Purohit et al., 2013). Hence, the reaction scheme for the 'gating' allosteric transition is $C_{LA} \rightleftarrows O_{HA}$. Without any bound agonists the probability of having the O_{HA} shape (P_O) is ~10^{-6} and baseline current is negligible (Jackson, 1986; Nayak et al., 2012; Purohit & Auerbach, 2009). With or without agonists, the receptor turns on and off spontaneously (influenced only by temperature). Agonists increase P_O (that is, preferentially stabilize O_{HA}) because they provide net favorable binding energy to their target when it is in the active, high-affinity conformation. Agonists also stabilize the transition state that separates C_{LA} from O_{HA} and therefore increase P_O almost exclusively by increasing the channel-opening rate constant.

The difference in binding free energies, HA minus LA (ΔG_{HA}-ΔG_{LA}), drives the receptor's allosteric transition and determines relative agonist efficacy (maximum P_O). Another ligand attribute we use is efficiency that is a function of the ratio of binding free energies, (1-$\Delta G_{LA}/\Delta G_{HA}$) (Nayak et al.,

57 2019). Efficacy (efficiency) is the amount (fraction) of binding free energy delivered to the gating
58 apparatus. In a dose-response curve, efficacy is manifest as the high-concentration asymptote and
59 efficiency as the correlation between this maximum and EC_{50}.

60 Adult-type muscle AChRs have 2 approximately equal and independent neurotransmitter sites
61 (Nayak & Auerbach, 2017). The net LA→HA binding free energy change (ΔG) for two neurotransmitters
62 (-10.2 kcal/mol) adds to that for the unfavorable unliganded isomerization (+8.3 kcal/mol at -100 mV)
63 (Nayak et al., 2012) making the free energy change of the allosteric transition with 2 bound ACh
64 favorable (-1.9 kcal/mol). ΔG is proportional to the logarithm of the corresponding equilibrium
65 constant (by -RT, where R is the gas constant and T the absolute temperature, equal to -0.59 at 23 ^{o}C).
66 Accordingly, after 2 neurotransmitters have bound, LA→HA rearrangements at the 2 orthosteric sites
67 increases P_O from ~10^{-6} to ~0.96 (Figure 1A).

68 The relationship between ΔG_{LA} and ΔG_{HA} binding free energies and the agonist properties
69 affinity, efficacy and efficiency are considered elsewhere (Auerbach, 2024). Here, our goal was to
70 associate the $\Delta G_{LA} \rightarrow \Delta G_{HA}$ change in binding free energy (4 agonists) with restructuring events at a
71 neurotransmitter site. Molecular dynamics (MD) simulations were used to explore conformational
72 changes in the LA→HA transition at the $\alpha-\delta$ neurotransmitter site of the *Torpedo* AChR (6UVW;
73 (Rahman et al., 2020)). In brief, binding free energies calculated *in silico* matched those estimated by
74 using electrophysiology *in vitro* (Indurthi & Auerbach, 2023), allowing the identification of LA versus HA
75 structures in the simulations. In the LA→HA transition for all agonists, three prominent
76 rearrangements were rotation (flip) of the ligand, downward displacement (flop) of loop C, and
77 compaction and stabilization of the binding cavity (fix). The initial LA and final HA conformations of the
78 site were connected by a brief intermediate state. The simulations suggest that the movement of a

79 weakly-bound agonist starts the change to strong binding and initiates the protein's allosteric
80 transition.
81
82 **Results**
83 *Hold.* Traditionally, receptor activation is divided into distinct stages called 'binding' (formation of a
84 ligand-protein complex) and 'gating' (receptor isomerization) (Figure 1). Here, we are concerned with
85 the connection between these stages as molecular movements at a neurotransmitter site.
86 In AChRs, agonist binding is a 2-step process. First, the agonist (A) diffuses to the target and
87 forms an encounter complex (A+C⇄A-C), after which a local 'catch' rearrangement establishes the LA
88 complex (A-C⇄AC_{LA}) (Jadey & Auerbach, 2012). Gating, too, involves multiple steps (Gupta et al., 2017;
89 Purohit et al., 2013). First, the site undergoes a local 'hold' rearrangement that establishes the HA
90 complex (AC_{LA}⇄AC_{HA}), after which other protein domains restructure without changing agonist affinity,
91 eventually opening the gate (Figure 1B).
92 The only agonist-dependent free energy changes in activation occur in the two local site
93 rearrangements, ΔG_{LA} (in catch) and $\Delta G_{HA}-\Delta G_{LA}$ (in hold). The terminal state in the 'binding' stage of
94 activation is AC_{LA} and the initial state in the 'gating' stage is AC_{HA}. Our interest here is hold, AC_{LA}⇄AC_{HA},
95 the local rearrangement that connects these two states. The free energy changes associated with the
96 other events in the activation sequence, namely the formation of the encounter complex and
97 downstream domain restructurings, are approximately the same for all agonists and so are not
98 relevant to this study.
99 Activation free energy changes incurred outside catch and hold, namely from the chemical
100 potential associated with encounter complex formation (Phillips, 2020) and from rearrangements in

101 other domains (and water), together represent an energy offset that is approximately agonist
102 independent. With a few exceptions, energy coupling between the agonist binding pocket and distant
103 residues (>15.0 Å) typically is weak (Gupta et al., 2017), so only the agonist's energy changes in catch
104 and hold determine the pharmacology attributes of affinity (ΔG_{LA} or ΔG_{HA}), efficacy ($\Delta G_{HA} - \Delta G_{LA}$) and
105 efficiency ($1-\Delta G_{LA}/\Delta G_{HA}$). In AChRs, ΔG_{LA} and ΔG_{HA} have been measured experimentally by using
106 electrophysiology for 23 agonists and 53 neurotransmitter site mutations (Indurthi & Auerbach, 2023).
107 Apo, resting-C with a bound toxin, and high-affinity desensitized AChR structures have been
108 solved by using cryo-EM (Rahman et al., 2022; Rahman et al., 2020; Zarkadas et al., 2022). Desensitized
109 AChRs have a similar (perhaps identical) high affinity as AO_{HA} (Auerbach, 2020; Nayak & Auerbach,
110 2017). Below, we describe the conformation dynamics that connect the end states of the hold
111 rearrangement, $AC_{LA} \rightarrow AC_{HA}$ (Figure 1B, bottom), neither of which has been captured as a structure.
112 However, as described below, they can be identified in MD simulations that use resting-C as a start.
113
114

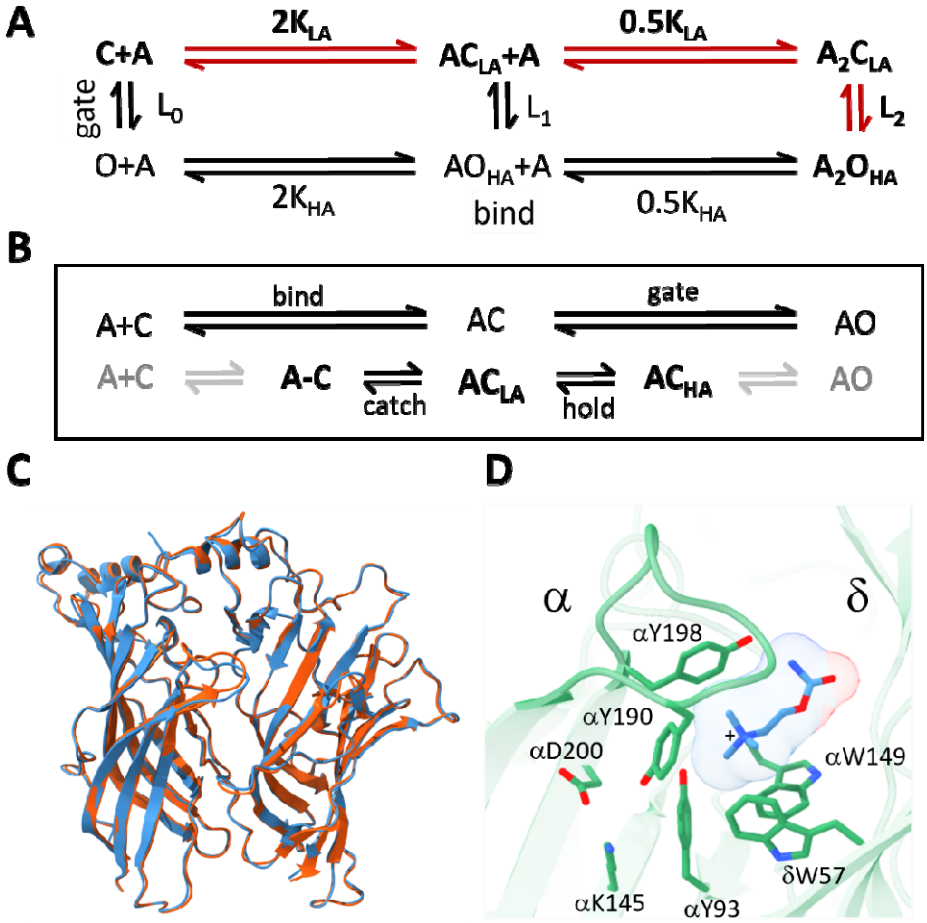

Figure 1: AChR activation. *A.* Cyclic, thermalized activation scheme (vertical, gating; horizontal, binding; red, main physiological pathway). Receptors isomerize globally between closed-channel/low-affinity (C_{LA}) and open-channel/high-affinity (O_{HA}) conformations (equilibrium constant L_n; n, number of bound ligands). Agonists (A) bind weakly to C_{LA} (equilibrium association constant K_{LA}, free energy change ΔG_{LA}) and strongly to O_{HA} (K_{HA}, ΔG_{HA}). In adult AChRs the 2 orthosteric sites are approximately equivalent and independent, and there is no significant external energy: $L_2/L_0 = (K_{HA}/K_{LA})^2$ (Nayak & Auerbach, 2017). B. Top, binding and gating. Bottom, catch and hold. The agonist diffuses to the target to form an encounter complex (A-C), a local 'catch' rearrangement establishes the LA complex (AC_{LA}), a local 'hold' rearrangement establishes the HA complex (AC_{HA}), the rest of the protein isomerizes without a further change in affinity to generate a conducting pore (AO). Gray, steps that incur the same energy change for all agonists used in this study; black, agonist-dependent free energy changes in catch is ΔG_{LA} and in hold (ΔG_{HA}-ΔG_{LA}). C. α-δ subunit extracellular domains, red, after toxin removal (6UWZ.pdb) and blue, apo (7QKO.pdb). There are no major deviations (C_α RMSD = 0.3 Å). D. Closeup of the desensitized *Torpedo* α-δ subunit neurotransmitter site occupied by carbamylcholine (CCh, blue) (7QL6.pdb; (Zarkadas et al., 2022)). In this is HA conformation, 3 aromatic groups in the α subunit (149-190-198) surround the agonist's cationic center (+) together provide ~90% of the binding energy for ACh (Purohit et al., 2014), and the tail points toward the δ subunit (*trans* orientation).

133 *Docking.* We began by removing α-bungarotoxin from the high-resolution (2.69 Å) structure 6UWZ
134 (Rahman et al., 2020) (Figure 1C) and docking agonists into the empty pocket. The docking simulations
135 had strong binding scores ranging from -5.82 to -9.18 kcal/mol (Figure 2A), suggesting that the
136 interactions were stable. However, unlike the agonist orientation apparent in cryo-EM structures of
137 desensitized (HA) AChRs (Noviello et al., 2021; Rahman et al., 2022; Rahman et al., 2020; Walsh et al.,
138 2018; Zarkadas et al., 2022) (Figure 1D), the docked agonist's tail pointed towards (*cis*) rather than
139 away (t*rans*) from the α subunit (Figure 2B, top). This was the case for the top 3 docking positions for
140 all 4 ligands.

141 Because the *cis* orientation was not observed in any cryo-EM structure, we examined the top
142 200 docking scores for CCh. All poses were *cis*, with the tail pointing towards the α subunit and away
143 from the main binding cavity. Apparently, in the apo structure the *trans* orientation is energetically
144 unfavorable. Hence, to start our analysis of the hold rearrangement we hypothesized that the agonist
145 orientations in the end states are *cis* in AC_{LA} versus *trans* in AC_{HA}.

146

147

148

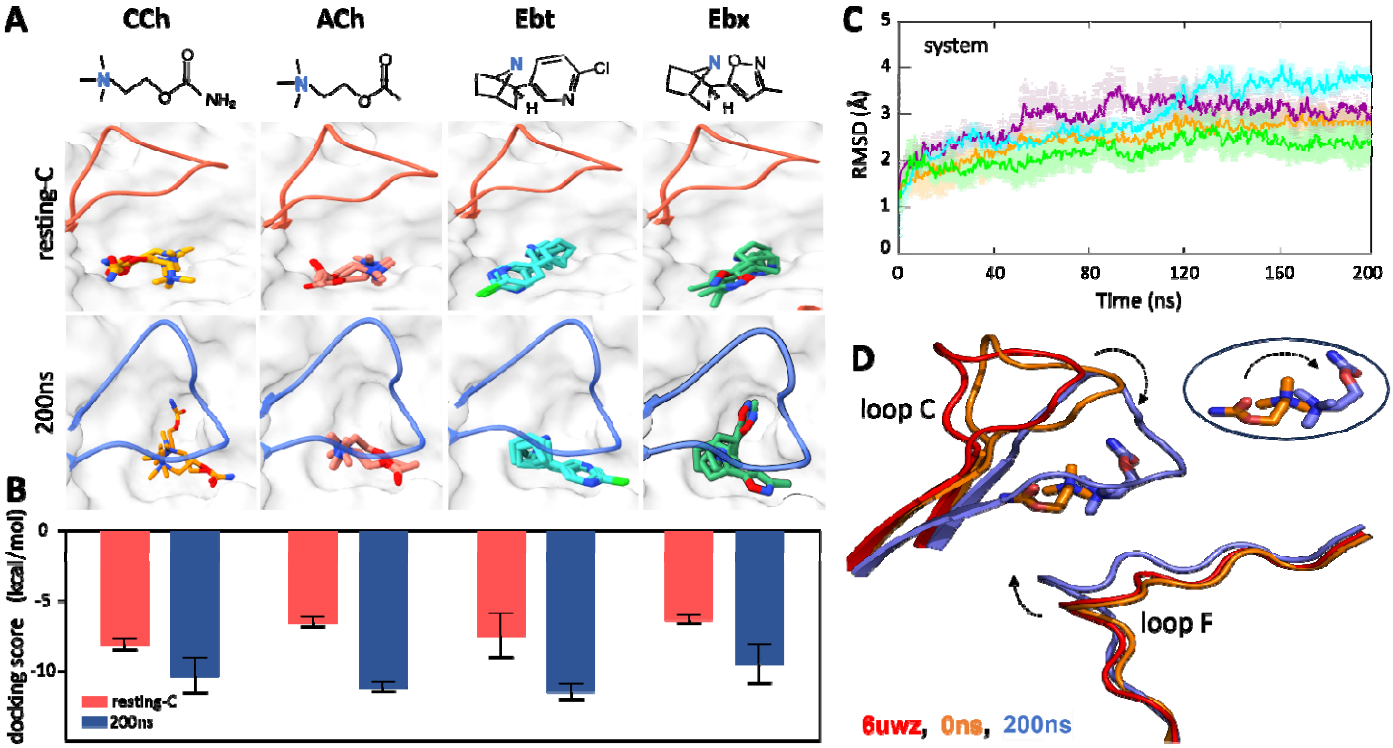

Figure 2. Agonist docking and loop dynamics. A. Top, agonists (blue, cationic center): carbamylcholine (CCh), acetylcholine (ACh), epibatidine (Ebt) and epiboxidine (Ebx). Bottom, $\alpha-\delta$ site (6UVW.pdb minus toxin, resting-C) with docked agonists (top 3 poses). docked into resting-C (red): loop C is up, agonist is *cis*. docked after 200 ns simulation and removing CCh (blue): loop C is down, agonist is *trans*. B. Bottom, docking scores (mean±SD, n=3). red, resting-C; blue, 200 ns. C. C_α RMSD (mean±SD, triplicates) (ACh, cyan; CCh, green; Ebt, orange; Ebx, purple). D. close-up of the CCh-occupied pocket. Red, resting-C; orange, equilibrated (0 ns); blue, 200 ns. After 200 ns loop C has flopped, loop F has moved inward, and the agonist has flipped *cis*→*trans*.

163 *The LA→HA transition*. We performed 200 ns MD simulations for each of the docked complexes, in
164 triplicate (with different seed values). Video 1 shows a simulation with CCh on 2 times scales,
165 expanded for the initial 200 ns and condensed for the full 1.0 μs extension. The 200 ns simulations for
166 all three replicates for all agonists showed similar root-mean-square-deviation (RMSD) patterns with
167 differences consistently below 1Å (Figure 2C, Figure 2-Source Data 1) suggesting that the trajectories
168 were sufficiently robust and reproducible. Although there were initial deviations, all systems became
169 stable by ~120 ns. The root-mean-square-fluctuation (RMSF) of the C_α atoms showed flexibility around
170 the pocket mainly in loops C and F (but not E) (Figure 2-figure supplement 1). The fluctuations at the
171 base of the ECD were anticipated because the TMD that offers stability here was absent. As described
172 below, the match between experimental binding energies (whole receptors) and those calculated in
173 the simulations (ECD dimers) is further evidence that the ECD-TMD interfacial region does not
174 influence agonist binding energy.

175 The ECD dimer in the absence of a bound agonist (apo) exhibited a similar RMSF and RMSD
176 pattern for a 200 ns simulation, to that observed with ligand present (CCh) (Figure 2-figure supplement
177 2A, Figure 2-figure supplement 2B). The displacement of loop C apparent with agonists (see below) was
178 also present but less pronounced in apo (Figure 2-figure supplement 2C).

179 In addition to the fluctuations in loops C and F during the simulations, the ligand orientation
180 inverted, *cis→trans*. For all ligands, at the start of the simulations the agonist's tail points towards α,
181 but by the end points towards δ (Figure 2D). The agonist re-orientation represents a nearly complete
182 somersault (a 'flip') about the agonist's main cationic center (N^+) that remains close to αW149
183 throughout (see Figure 5). The final MD configuration (with CCh) aligns well with the CCh-bound cryo-
184 EM desensitized structure (7QL6.PDB) (RMSD < 0.5 Å) (Figure 2-figure supplement 3). Video 1 shows

185 that the final *trans* orientation with CCh remains constant for at least 1 μs, indicating that structure
186 had settled by 200 ns, with critical rearrangements conserved.

187 To test whether rearrangements at the binding pocket in the simulations enforced the *trans*
188 configuration, we removed the bound CCh from the final 200 ns MD structure and re-docked the
189 agonists. The preferred poses for all 4 ligands were *trans* (Figure 2A, bottom). In addition, binding
190 energies from docking scores were higher for the 200 ns structures compared to the initial binding site
191 structures, consistent with a LA-to-HA transition (Figure 2B). As a further control we carried out MD
192 simulations of a pentamer docked with ACh and found similar structural changes at the binding pocket
193 compared to the dimer (Figure 2-figure supplement 4).

194 Together, these results suggest that ECD dimers are adequate to study local rearrangements of
195 the α–δ AChR neurotransmitter binding site. Further, they provide support for the hypotheses that in
196 the simulations the site restructures from AC_{LA} to AC_{HA}, and that the preferred agonist pose is *cis* in LA
197 versus *trans* in HA structures.

198

199 *Principal component analysis (PCA)*. To identify the most prominent conformational states of the
200 receptor during the simulations, PCA was carried out based on the most significant fluctuations
201 (principal components). Considering the first two principal components (PC-1 and PC-2) that captured
202 the most pronounced C_α displacements (Figure 3-Source Data 1), backbone fluctuations revealed three
203 energy minima (m1, m2, and m3) that reflect the stabilities of loops C and F (Figure 3). To assess
204 consistency across independent simulations, we calculated the inner products of the top 10 principal
205 components from each run. The resulting heatmaps reveal the degree of similarity between runs, with

206 the inner product values of PC-1 and PC-2 reflecting considerable overlap (50-90%) in the principal
207 dynamic modes captured in each simulation (Figure 3-figure supplement 1).

208 For all 4 agonists, trajectories started in m1 and ended in m3 (Figure 3-figure supplement 2).
209 Accordingly, we hypothesized that m1 corresponds to AC_{LA} and that m3 corresponds to AC_{HA}. For all
210 agonists, the m2 population had a greater variance (was less stable) compared to m1 and m3. This,
211 along with its temporal position, suggests that m2 represents an unstable intermediate configuration
212 within the hold transition, between AC_{LA} and AC_{HA}. For all agonists and trajectories, m3 had the least
213 variance (was the most stable).

214 The pronounced fluctuations in loop C are evident in residue-wise RMSF plots and align well
215 with the contributions of the first two principal components (PC-1 and PC-2) (Figure 2-figure
216 supplement 2D). The apo and CCh occupied proteins adopt similar conformational spaces during the
217 200 ns simulation (Figure 2-figure supplement 2E). However, presence of the agonist appears to
218 increase conformational diversity, generating a broader distribution in the PCA plot. The bottom of the
219 m1, m2 and m3 energy wells in Figure 3 represent the most stable configurations of each population
220 and serve as reference points.

221

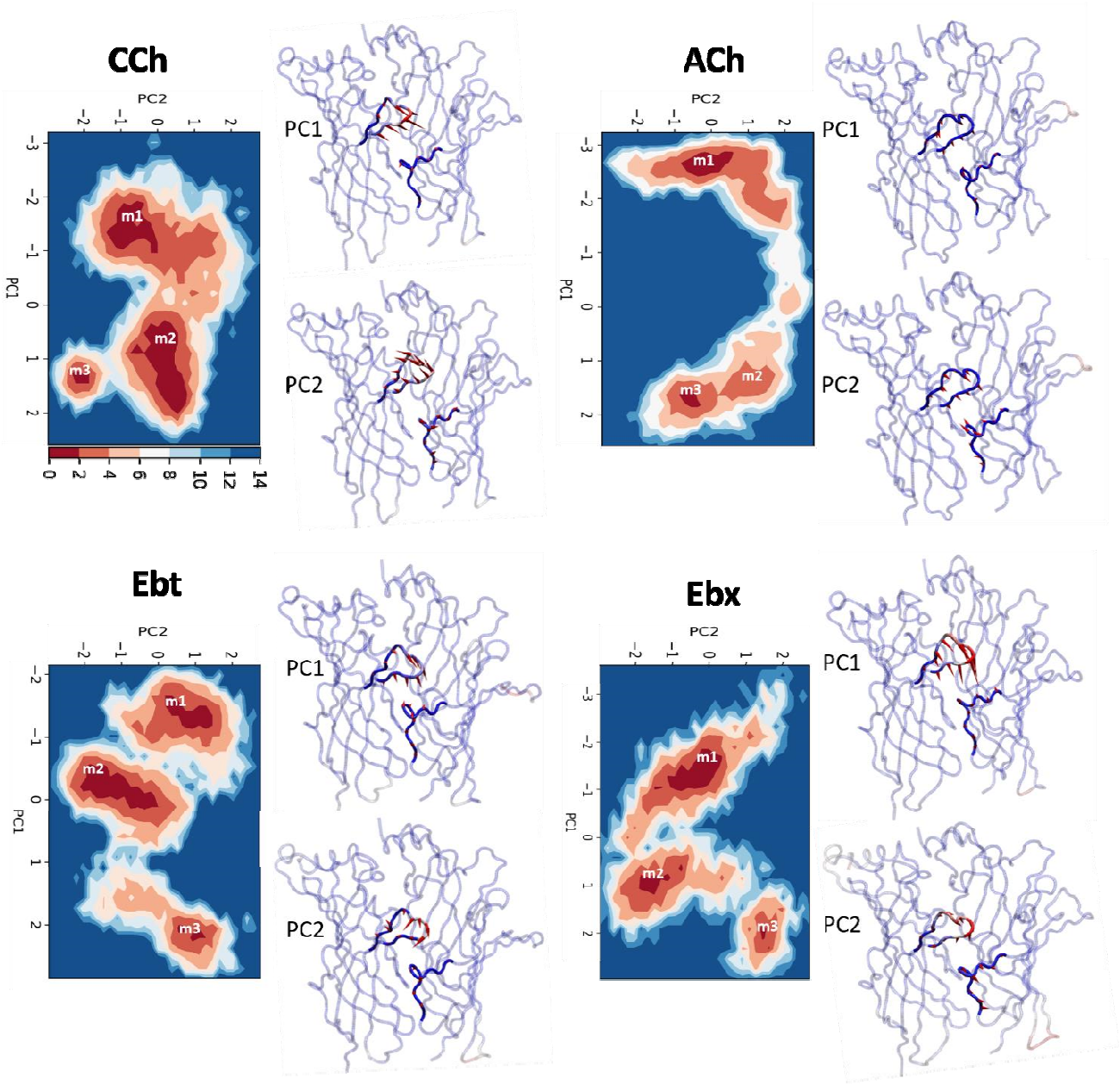

202

Figure 3. Principal Component Analysis (PCA). For each agonist, the left panel plots PC1 vs PC2, the first two principal components that capture the maximum variance in the trajectory (Figure 3-Source Data 1). Colors represent free energy value in kcal/mol (scale, upper left-bottom). For all agonists there are 3 energy minima (dark red), m1, m2, and m3, that correspond to different conformations of the protein. The right panels are 'porcupine' plots indicating that the direction and magnitude of changes between PC1 and PC2 is in loops C and F. From energy comparisons (Figure 4, Figure 4-Source Data 1) and temporal sequences (Figure 3-figure supplement 2, Figure 4-Source Data 1): m1 is AC_{LA}, m3 is AC_{HA}, and m2 is an intermediate configuration.

232 *Computed versus experimental binding energies.* Although the well bottoms in Figure 3 represent the
233 most stable overall conformations, they do not directly convey information regarding agonist stability
234 or orientation. To incorporate this information, we performed a cluster analysis of the ligand
235 configuration using frames from the bottom of each PCA well as input. The top three clusters, each
236 having RMSD of ≤ 1.0 Å, shared a similar ligand orientation (Figure 3-figure supplement 2) and were
237 selected to compute binding free energies (Figure 4, Figure 4-Source Data 1, Figure 4-Source Data 2).
238 The remaining frames were disregarded. The fraction of frames from each minimum accepted for free
239 energy calculations ranged from 20% (ACh, m1) to 71% (Ebt, m3). On average, the fraction of frames
240 selected was ~50%, showing the dynamic nature of the ligand in the pocket (Video 1).

241 The above procedure defined populations of structures that we hypothesized represent the end
242 states of hold, AC_{LA} (m1) and AC_{HA} (m3), plus a previously unidentified intermediate state (m2). We
243 used PBSA (Poisson-Boltzmann Surface Area) computations of the selected structures for each agonist
244 in each cluster population and compared binding free energies calculated *in silico* with those measured
245 previously *in vitro* (Indurthi & Auerbach, 2023). There are limitations with regard to PBSA accurately
246 predicting absolute binding free energies (Genheden & Ryde, 2015; Hou et al., 2011) that also depend
247 on parameterization of the ligand (Oostenbrink et al., 2004). However, because we knew the actual
248 binding free energies from electrophysiology experiments we used the PBSA calculations only to test
249 our hypothesis that m1 is AC_{LA} and m3 is AC_{HA}.

250 Calculated PBSA and experimental ΔG values are compared in Figure 4A left (Figure 4-Source
251 Data 1). For ACh and CCh there was good agreement between ΔG_{m1} and ΔG_{LA} and between ΔG_{m3} and
252 ΔG_{HA}. For these agonists, *in silico* values overestimated experimental ones by ~8% and ~25%. The
253 agreement was not good for the other 2 agonists, with calculated values overestimating experimental

254 ones by ~45% (Ebt) and ~130% (Ebt). However, in all cases ΔG_{m3} was more favorable than ΔG_{m1}, and
255 the % overestimation was approximately the same for m1 versus m3. Despite the mismatches with the
256 PBSA calculations, the comparison is consistent with the hypothesis.

257 Further support for the assignments comes from comparing calculated vs experimental
258 efficiencies that depend on the binding free energy ratio, $\Delta G_{LA}/\Delta G_{HA}$, rather than absolute ΔGs. As
259 described elsewhere, efficiency is the agonist's free energy change in hold relative to its total free
260 energy change, $(\Delta G_{HA}-\Delta G_{LA})/\Delta G_{HA}$ or $(1 -\Delta G_{LA}/\Delta G_{HA})$ (Nayak et al., 2019). Figure 4A right (Figure 4-
261 Source Data 1) shows that efficiency values calculated *in silico* agree almost perfectly with those
262 measured experimentally. This result not only further supports the hypothesis that m1 represents AC_{LA}
263 and m3 represents AC_{HA}, but also indicates that efficiency can be computed from structure alone. We
264 conclude that MD simulations of a single pdb file successfully model the end states of the hold
265 transition and that the trajectories likely reproduce the conformational dynamics in $AC_{LA}\rightarrow AC_{HA}$.

266 All agonists show an increase in van der Waals (VdW) interaction energy in this rearrangement
267 (Figure 4B). The calculated increase (PBSA calculations) was most pronounced with Ebt and least for
268 Ebx, with CCh and ACh falling in between (Figure 4-Source Data 2). $AC_{LA}\rightarrow AC_{HA}$ restructuring of the
269 binding pocket generates a smaller, more-tightly packed pocket (Tripathy et al., 2019), in part because
270 of the increased VdW interactions (Video 1). This is shown in Figure 4C as a reduction in binding pocket
271 volume and in Figure 4D as a decrease in the number of water molecules. The VdW contacts that form
272 concomitant to agonist flip and loop C flop establish a more compact, hydrophobic and stable local
273 environment (Video 1).

274

275

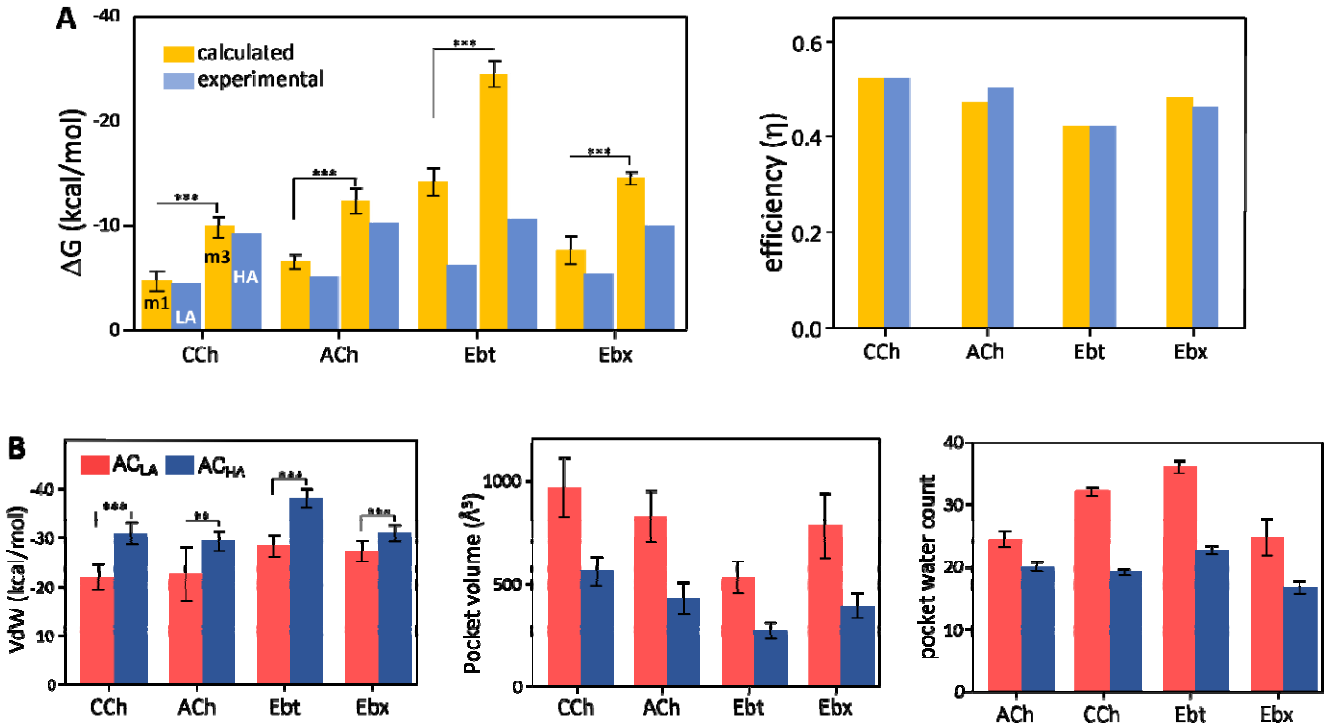

Figure 4. Binding free energies and pocket properties. A. Calculated (yellow) versus experimental (blue) binding free energies for 4 agonists (Figure 2A, top) (Figure 4-Source Data 1). PBSA calculations were done on clusters selected from m1 and m3 minima of PCA plots (Figure 3; Figure 3-figure supplement 2). Left, absolute ΔG and right, efficiency. The agreement in efficiencies supports the hypothesis that m1 represents AC_{LA} and m3 represents AC_{HA}. B. In $AC_{LA} \rightarrow AC_{HA}$, VdW interactions increase (left), pocket volume decreases (center) and the number of water molecules decreases (right). Overall, the pocket stabilizes, compacts and de-wets.

284 *Flip-Flop-Fix*. In AC_{LA}→AC_{HA}, a *cis*→*trans* rotation of the agonist (flip) was prominent in all simulations

285 (Figure 5). All agonists underwent a >130° rotation about the N^+-αW149 fulcrum. Also, in all instances

286 the flip occurred near the start of the hold rearrangement.

287 A second consistent and prominent restructuring event in AC_{LA}→AC_{HA} was the downward

288 displacement (flop) of loop C toward the pocket center (C_α of αW149). This well-known 'clamshell

289 closure' motion is conserved in related binding proteins and thought to play a role in AChR activation

290 by agonists (Basak et al., 2020; Hansen et al., 2005; Hibbs et al., 2009). In the simulations, loop C flop

291 was measured as the displacement of its tip (C_α of αC192) in m3 relative to its apo position. The

292 distance traveled varied with the agonist (Figure 6-table supplement 1) but we do not discern a pattern

293 in the extent of loop C flop with regard to agonist affinity, efficacy or efficiency.

294 In hold, residues that form the pocket cavity move, presumably to accommodate the reoriented

295 ligand. In AC_{LA}, αY190, αY93, and δW57 are spaced apart, providing an open slot that accommodates

296 the agonist's tail in the AC_{LA}, *cis* orientation (Figure 5- figure supplement 1). However, in AC_{HA} loop C

297 flop repositions αY190 closer to αY93, effectively filling the gap to create a unified surface.

298

299

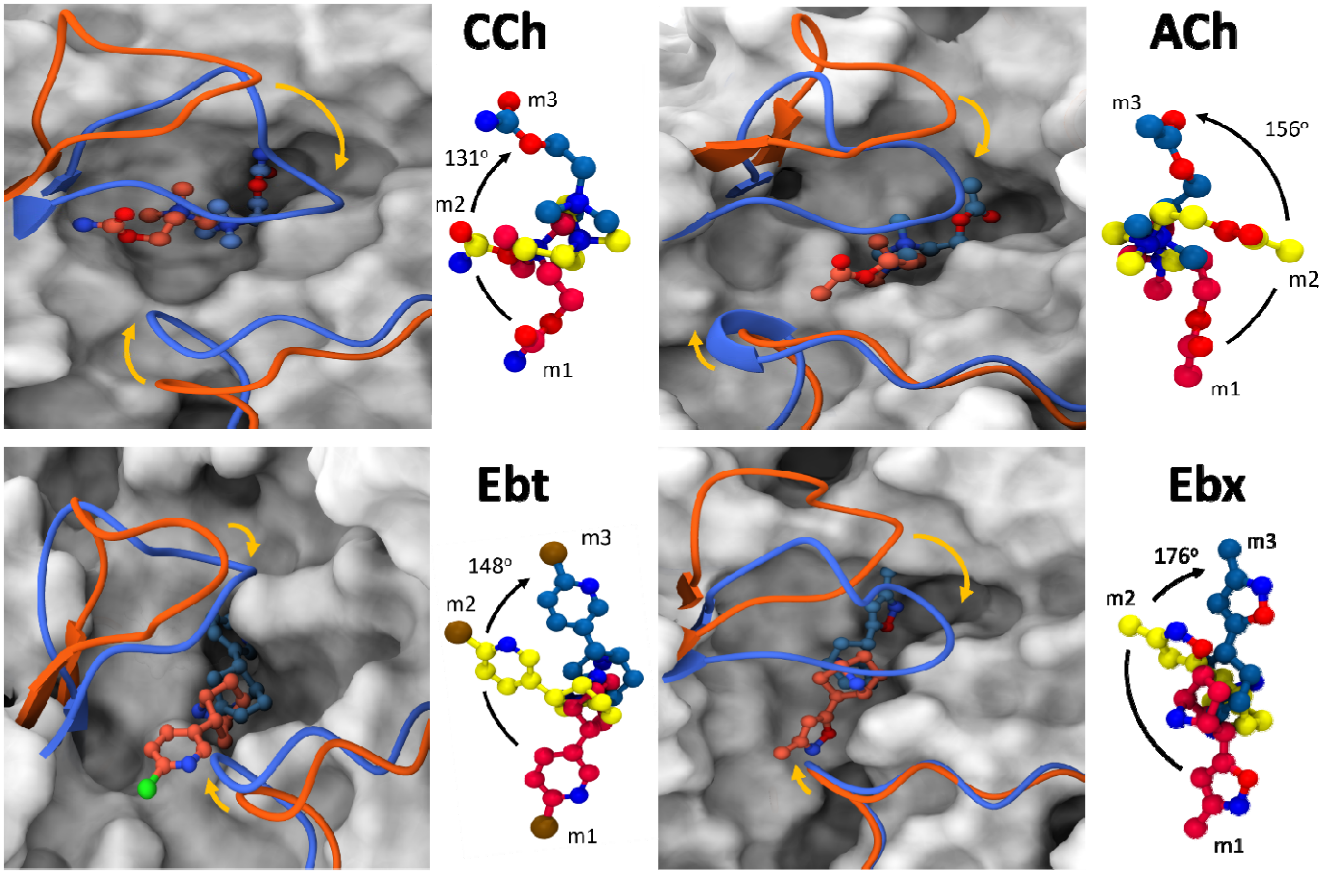

Figure 5. Agonist and loop movements in hold. In each panel *left*, superimposed cartoons of AC_{LA} (m1; orange) and AC_{HA} (m3; blue). Loop C is upper left and loop F is lower right. In AC_{LA}→AC_{HA} (red→blue) there is a *cis*→*trans* reorientation of the agonist (a flip) and a downward movement of loop C (a flop, orange arrow); *right*, flip from m1 (red) to m2 (yellow) to m3 (blue); degree, m1→m3.

307 The αW149, αY190, αY198 and αY93 rings surround the N^+ (Figure 1D). In adult-type mouse
308 AChRs, Ala substitutions of these 4 aromatic residues have different consequences and result in ACh LA
309 binding free energy losses of 3.0, 2.7, 2.2 and 1.1 kcal/mol, respectively (Purohit et al., 2014). δW57A
310 does not change ACh binding energy (Nayak & Auerbach, 2013). αW149 (in loop B) makes a cation-π
311 bond with N^+ that is important for ligand stabilization (Xiu et al., 2009; Zhong et al., 1998). In the
312 simulations, the distance between αW149 and N^+ decreases only slightly, AC_{LA}→AC_{HA} (Figure 6, Figure
313 6-table supplement 1). This cation-π bond appears to act as a slippery anchor (a hinge) that maintains
314 stability of the N^+ position even as the tail rotates about it.

315 In AChBP (perhaps C_{LA}), the hydroxyl group of αY93 forms a hydrogen bond with the ligand
316 head group (Celie et al., 2004; Hansen et al., 2005). In the AChR AC_{LA} structure, the *cis* orientation
317 appears to be stabilized by this hydroxyl as it is close to a functional group on the agonist's tail.
318 Likewise, the tail nitrogen in CCh, Ebt, and Ebx (amide or amine) forms a hydrogen bond with the
319 hydroxyl group of αY198, but only in the intermediate m2 state. This interaction may guide the flip and
320 provide transient stability. The absence of a secondary nitrogen in ACh possibly explains its alternate
321 re-orientation route, as only this ligand was observed to flip counterclockwise (Figure 5). It may also
322 explain why the m2 basin in the PCA plots for ACh is especially broad and shallow (Figure 3).

323 The AC_{LA}→AC_{HA} transition compacts, dehydrates and stabilizes the binding cavity (Figure 4;
324 Video 1). In AC_{HA}, the tail functional moiety (carbonyl or secondary ring amine) in the *trans* orientation
325 is sandwiched between αC192, αC193 and αY198 (loop C), αT150 (loop B) and δC108, δN109, δL111,
326 and δL121 (loop E) (Figure 6- figure supplement 1). As reported elsewhere (Blum et al., 2010; Rahman
327 et al., 2020; Zarkadas et al., 2022), in AC_{HA} the functional group found in the tail of each agonist -- the
328 carbonyl group in CCh and ACh and the secondary ring amine in Ebt and Ebx - forms a hydrogen bond

329 with the carbonyl of δN109 and amine of δL121 in the complementary δ subunit backbone *via* a
330 structural water (Figure 6). The agonist's flip occurs at the start of m1→m2, and the establishment of
331 this water-mediated H-bond completes in m2→m3 (Figure 6) (Video 1). This water-mediated bonding
332 and the increase in VdW interactions appear to both be crucial for stabilizing the loops and agonist in
333 the HA conformation of the neurotransmitter site.
334
335 *Salt-bridge*. Near the pocket, the αK145-αD200 salt bridge (Figure 1D) has been suggested to play an
336 important role in receptor activation (Beene et al., 2002; Gay & Yakel, 2007; Mukhtasimova et al.,
337 2005; Padgett et al., 2007; Pless et al., 2011). The hold rearrangements of αK145 are complex and
338 agonist dependent. In AC_{HA}, this residue i) makes an apparent contact with αY93, ii) contacts the αY190
339 hydroxyl group (Figure 6-table supplement 1) and, iii) approaches loop F of the complementary
340 subunit.
341 Interestingly, the mutation αK145A lowers the efficiencies of ACh and CCh (from 0.51 to 0.41)
342 but has no effect on those of Ebt and Ebx (0.41 and 0.46) (Indurthi & Auerbach, 2023). This agonist
343 dependence in function has a parallel in structure. In the hold simulations, the αK145-αD200 distance
344 (Å) increases from only 4.4 in apo to 6.1 or 5.1 in AC_{LA} (CCh or ACh). This spreading may relate to the
345 agonist's tail being inserted into the αY93 slot in the *cis* orientation. In AC_{LA}→AC_{HA}, for some agonists
346 the αK145-αD200 separation (Å) shortens substantially to 2.8 or 2.6, making it more rigid (ACh or CCh).
347 However, with Ebt and Ebx the αK145-αD200 distance remains unstable, fluctuating between 3-6 Å
348 throughout the course of the simulation. Likewise, αK145-αY190 distance stabilizes at 5.3 Å or 6.1 Å in
349 AC_{HA} with ACh and CCh but continues to fluctuate with Ebt and Ebx. In contrast, the αY190-αD200

distance remains stable in AC_{HA} for all ligands. This suggests that the instability in the αK145-αD200 and αK145-αY190 distances can primarily be attributed to αK145 (Figure 6- figure supplement 2).

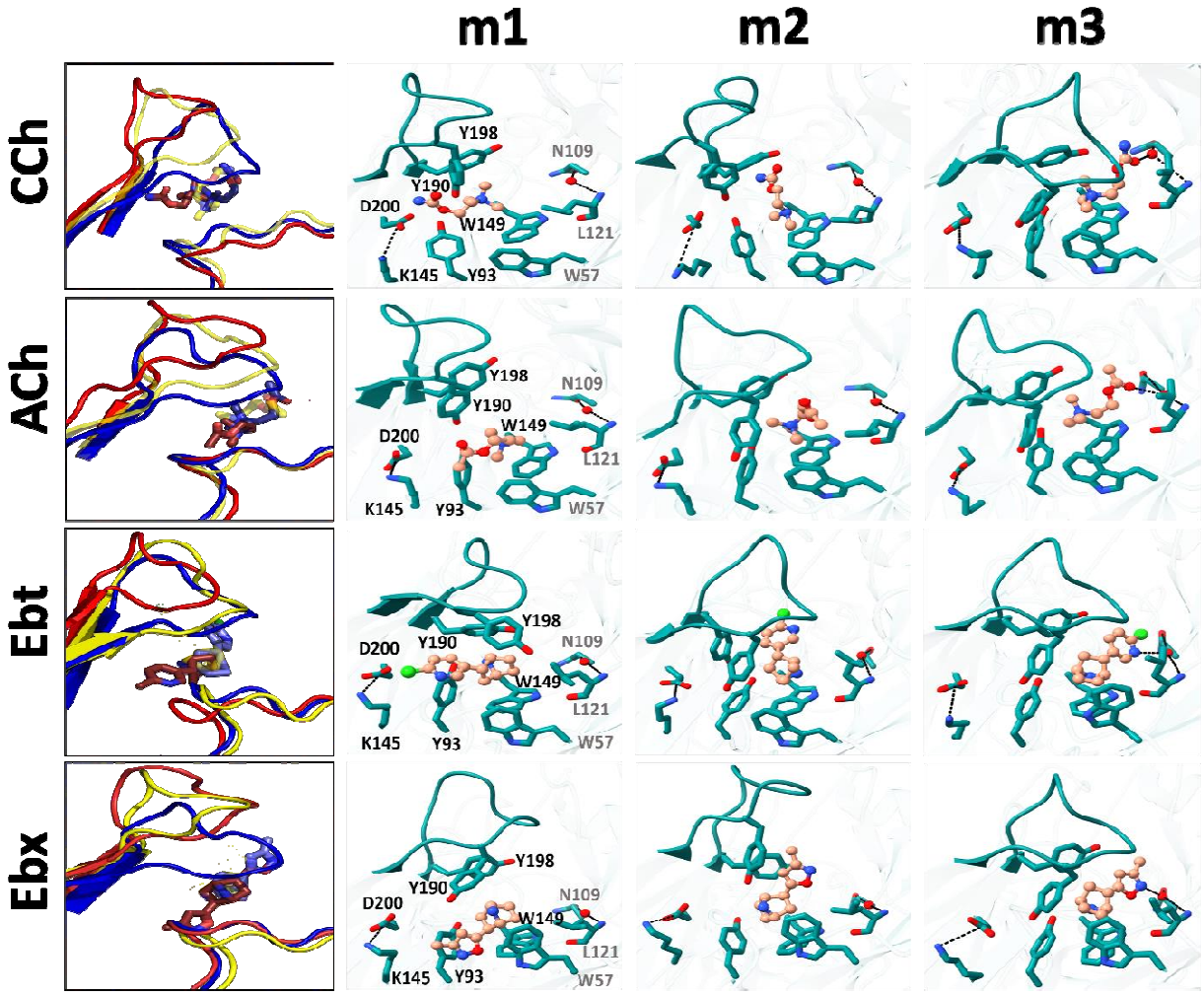

Figure 6: Representative snapshots in AC_{LA}→AC_{HA} (hold). *left*, rearrangements of loop C, loop F and the ligand (red, m1; yellow, m2; blue, m3); *right*, residue and ligand orientations. m1 is AC_{LA} , m2 is an intermediate state, m3 is AC_{HA}. In m1, a functional group in the agonist tail interacts with αY93 (all agonists) and αD200 (only CCh and Ebt). The position and orientation of αW149 relative to N^+ of the agonist remains nearly unchanged m1→m2→m3 and serves as a fulcrum for the *cis*→*trans* flip (see Figure 5). In m2, the functional nitrogen at the agonist tail (CCh, Ebt and Ebx) interacts with the hydroxyl group of αY198. For all ligands, αY190 repositioning and loop C flop (m1→m3) are correlated. In m3, the agonist fully flips to *trans*, facilitating VdW interactions, de-wetting, and the formation of water-mediated hydrogen bonds with the reactive group at its tail with δN109/δL121 backbone (loop E) via a structural water.

364 **Discussion**

365 After diffusing to the target, the only agonist-dependent rearrangements (energy changes) in
366 receptor activation are in catch and hold, A-C⇄AC_{LA}⇄AC_{HA} (Figure 1B, bottom) (Auerbach, 2024; Jadey
367 & Auerbach, 2012). By comparing binding energies calculated *in silico* with those measured *in vitro* we
368 were able to identify in the MD trajectories the hold end states, AC_{LA} and AC_{HA}, plus an intermediate
369 configuration not detected in electrophysiology experiments. Three conspicuous hold rearrangements
370 discussed below are: i) a *cis*→*trans* rotation of the agonist (flip), ii) an up→down displacement of loop C
371 (flop), and iii) reductions in pocket volume, water and fluctuations (fix).

372 There was reasonably good agreement between calculated and experimental binding free
373 energies for ACh and CCh, but the match was excellent when free energy ratios (efficiencies) rather
374 than absolute values were compared (Figure 4A). Absolute *in silico* values overestimated experimental
375 ones by approximately the same factor (different for each ligand) that cancelled in the ratio. We do not
376 know the origin of this factor but speculate that it is caused by errors in ligand parameterization.
377 Regardless, the results show that agonist efficiency can be a useful metric for associating structure
378 with function, and that efficiency can be estimated from structure alone.

379 Below we consider the structural elements associated with flip, flop and fix, namely the agonist
380 (*cis*→*trans*), loop C (up→down) and the pocket (large→small, *et al*). MD simulations of the α–δ AChR
381 neurotransmitter site suggest the following approximate and jittery generic sequence of
382 rearrangements in AC_{LA}→AC_{HA} (Video 1). The stable states are bold.

383 1. **AC_{LA} (m1)**: agonist *cis*, loop C up, pocket wide/wet/wobbly,
384 2. ...agonist leaves *cis* and starts to rotate about the N^+-αW149 fulcrum,
385 3. ...loop C starts to move down (towards the fulcrum).

4. **Intermediate (m2)**: agonist half-rotated, tail stabilized by αY198,
5. ...agonist rotates to *trans* (little change at the fulcrum), tail not secured in the pocket,
6. ...loop C is fully down.
7. **AC_{HA} (m3):** agonist *trans*, tail secured by VdW contacts and H-bonds, pocket small/dry/rigid.

Agonist. With all agonists and in all simulations, the rotation of the agonist about the N^+-αW149 fulcrum begins at the start of the $AC_{LA} \rightarrow AC_{HA}$ transition. Movements of bound ligands have been identified in other proteins. In AMPA-type glutamate receptors, the neurotransmitter glutamate binds in either of 2 poses, crystallographic or inverted (Yu et al., 2018). In one MD simulation these interconverted, suggesting the bound ligand is not rigidly fixed. Although the alternative poses were not associated with binding energies, the binding cleft was more closed in the crystallographic (presumably HA) versus inverted (possibly LA) orientation. The re-orientation of a bound glutamate in AMPA receptors is possibly related to the flip of the agonist in AChRs.

Multiple ligand positions in binding pockets have also been reported in Glycine receptors (Yu et al., 2014), 5-HT3 receptors (Basak et al., 2020), δ-opioid receptors (Shang et al., 2016), HIV-1 protease (Klei et al., 2007) and transthyretin (Klabunde et al., 2000). In enzymes, bound substrate movement is apparent in hexokinase (Bennett & Steitz, 1978) and alcohol dehydrogenase (Plapp, 2010). It is not unusual for movement of a bound ligand to trigger an otherwise unfavorable local rearrangement that drives protein function (an 'induced fit'; (Richard, 2022). Not only can an untethered ligand come and go, it can also reorient itself dramatically to change binding energy and, hence, the local environment that couples to the full allosteric transition.

407 In AChRs, such ligand reorientation cannot pertain to all agonists. Some with high potency are
408 perfectly symmetrical (decamethonium) and some lack a tail (tetramethylammonium). Although we
409 have not yet identified the conformational dynamics that determine ΔG_{HA}, factors other than the flip
410 certainly contribute, and in proportions that are likely to be agonist dependent (see below).

411 The PCA plots (Figure 3) show 3 structural populations, one of which (m2) occurs in time
412 between m1 (AC_{LA}) and m3 (AC_{HA}) (Figure 3-figure supplement 2). In m2, the agonist's tail (CCh, Ebt and
413 Ebx) interacts with αY198, possibly to guide the clockwise rotation of the ligand and reduce the
414 probability of a return to the *cis* orientation. The PBSA calculations indicate that ΔG_{m2} (that does not
415 have an experimental correlate) is intermediate between ΔG_{LA} and ΔG_{HA} for ACh and CCh, but least
416 stable for Ebt and Ebx (Figure 4-Source Data 1). We do not have an explanation for this difference.

417

418 <u>*Loop C.*</u> A number of observations place focus on the role of the downward displacement of loop C in
419 receptor activation. In ACh binding proteins, its extent correlates with agonist potency (Basak et al.,
420 2020; Du et al., 2015; Polovinkin et al., 2018) even if voltage-clamp fluorometry of other receptors
421 shows it to be similar with agonists and antagonists (Chang & Weiss, 2002; Munro et al., 2019; Pless &
422 Lynch, 2009). Simulations of the apo AChR indicate that in the absence of agonists loop C has flopped
423 partially, narrowing the aqueous connection between the bath and the pocket (Figure 2-figure
424 supplement 2C).

425 Given the flop in loop C, it is puzzling that electrophysiology measurements show the agonist
426 association rate constant (k_{on}) is substantially *faster* to C_{HA} (narrow entry, loop C down) than to C_{LA}
427 (wide entry, loop C up), as well as more correlated with agonist potency (Grosman & Auerbach, 2001;
428 Nayak & Auerbach, 2017). Docking results offer a clue to the apparent contradiction that narrowing an

429 entrance speeds association up to the diffusional limit (4 x10^9 $M^{-1}s^{-1}$). All 4 agonists dock in the *cis*
430 orientation to C_{LA} (wide) versus in the *trans* orientation to C_{HA} (narrow) (Figure 2B). Hence, despite the
431 wider aperture, *trans* is disfavored and lower affinity *cis* is preferred. We hypothesize that binding in
432 the *trans* orientation is prohibited in the apo pocket, and that loop C flop (and other rearrangements)
433 both narrow the entrance and remove this prohibition. Accordingly, k_{on} with loop C up (LA) is slower
434 than with loop C down (HA). We do not know the structural element(s) that prohibits *trans* with a wide
435 pocket. Any or all of the constellation of rearrangements in unliganded $C_{LA}\rightarrow C_{HA}$ could contribute.

436 As an aside, the inward displacement of loop C toward the pocket center resembles the
437 'clamshell closure' apparent at other receptor binding sites (Chen et al., 2017; Hansen et al., 2005;
438 Hibbs & Gouaux, 2011). However, in light of the k_{on} experimental results, using 'closure' (or 'capping')
439 to describe this motion is misleading because it implies putting a lid on the pocket that would reduce,
440 not increase, the agonist association rate constant. For this reason, we use functionally neutral words
441 'flop' and 'up/down' for loop C displacement and position.

442 AChRs can turn on without a loop C. Truncation of loop C eliminates activation by ACh but has
443 almost no effect on unliganded activation (Purohit & Auerbach, 2013). Interestingly, leaving only loop
444 C residues αY190 and αY198 in place saves activation by ACh. Hence, repositioning of one (or both) of
445 these in up→down is sufficient to maintain activation by the neurotransmitter. Other agonists were
446 not investigated.

447 αY190 is our interest. An Ala substitution here results in a large loss of ACh binding energy
448 with about half coming from the removal of the hydroxyl group (Purohit et al., 2014). In contrast, the
449 mutations αY198F and αY93F have essentially no effect on ACh binding energy. These results suggest
450 that repositioning αY190 consequent to loop C flop is important for activation by ACh (Figure 6). The

451 αY190 ring fills the slot that opens next to αY93 when the agonist exits *cis*, preventing a return (Figure
452 5-figure supplement 1). However, the distance between the αY190 ring and N^+ does not change
453 significantly so it is unlikely that the deployment of αY190 increases binding energy *via* an interaction
454 with the ring (Figure 6-table supplement 1).

455 Perturbation of the salt bridge residue αD200 by the αY190 hydroxyl has been proposed to
456 trigger the AChR allosteric transition (Beene et al., 2002; Gay & Yakel, 2007; Mukhtasimova et al.,
457 2005; Padgett et al., 2007; Pless et al., 2011). In support of this idea, the mutation αK145A reduces
458 ACh (and choline) binding energy substantially but has no effect when the αY190 hydroxyl is absent
459 (Bruhova & Auerbach, 2017). In the simulations, the downward displacement of loop C positions the
460 αY190 hydroxyl to within ~5.0 Å of αD200 and αK145 (Figure 6-table supplement 1). We sought, but
461 did not find, structural water in this gap. Although there was no correlation between these separations
462 and the degree of loop C displacement, the gap was smaller with high- (ACh and CCh) versus low-
463 efficiency agonists (Ebt and Ebx). In summary, some evidence supports the above proposal, but so far,
464 the simulations have not illuminated a mechanism. Substrate-induced loop displacements are known
465 to deploy residues to enhance catalysis, for example in chymotrypsin (Ma et al., 2005) and
466 triosephosphate isomerase (Brown & Kollman, 1987; Nickbarg et al., 1988). Repositioning αY190 in the
467 AChR $AC_{LA} \rightarrow AC_{HA}$ transition could be analogous.

468 Although attention on loop C has focused on the role of the flop, it is also important to consider
469 the functional consequences of the up position. The structural elements of the up (wide cleft)
470 configuration that prohibit agonist docking into the *trans* orientation have not been identified. A key
471 requirement for allostery is that the ligand bind more strongly to one of the alternative conformations
472 of the orthosteric site, so attention must also be given to the conformational dynamics of the 'catch

473 rearrangement, A-C⇄AC_{LA}. In both $GABA_A$ (Jones et al., 2001; Mortensen et al., 2010) and ACh
474 receptors (Jadey & Auerbach, 2012) the LA agonist association rate constant is correlated with potency
475 rather than diffusion constant, indicating that the formation of AC_{LA} requires an energy (structure)
476 change.
477
478 Pocket. The αW149-N^+ hinge remains relatively unchanged in the hold transition (Figure 6, Figure 6-
479 table supplement 1). Hence, we hypothesize the bulk of the extra favorable agonist binding energy in
480 AC_{HA} is not generated here but somewhere else, *cis→trans*. For the agonists we examined, the rotation
481 places the tail into the main binding cavity (Figure 6-figure supplement 1) (Video 1). The *trans*
482 orientation is secured by VdW interactions (possibly caused by further downward loop C displacement
483 and dehydration) and a hydrogen bond with a structural water bonded to the loop E backbone (in the
484 complementary subunit). The net result to the overall pocket is a reduction in volume (Figure 4C) and
485 increase in stability of loops C and F (Figure 3).
486 In the simulations, these two structural changes, distributed over the large surface area of the
487 cavity, were robust and consistent for all 4 agonists. It is possible that the increase in binding free
488 energy in hold derives mainly from restructuring of the pocket rather than from a change in the N^+-
489 aromatic interactions or, indeed, any one local ligand-protein interaction. Compact, hydrophobic
490 binding pockets are associated with functional activation in other ion channels (Furukawa et al., 2005;
491 Sigel & Steinmann, 2012) and observed in other proteins including β2-adrenergic receptors, opioid
492 receptors, and HIV-1 protease (Huang et al., 2015; Rasmussen et al., 2011; Wlodawer & Erickson,
493 1993).

494 After hold, the next step In AChR gating is the rearrangement of the extracellular domain
495 (Auerbach, 2024; Purohit et al., 2013). In related receptors, this domain becomes more compact and
496 stable (a rearrangement called 'unblooming') (Sauguet et al., 2014; Taly et al., 2009), structural
497 changes that echo those in hold at the AChR neurotransmitter site. It is therefore possible that the
498 $AC_{LA} \rightarrow AC_{HA}$ rearrangement of the neurotransmitter site nucleates the subsequent restructuring of the
499 extracellular domain. Extending this speculation, the structural correlates of energy change in gating
500 might at first spread in contact area (from N^+, to pocket, to extracellular domain) and then refocus
501 (from transmembrane domain, to gate region, to pore water).

502 In the complementary δ subunit (Figure 1D), loop E (β5-β6 strands) has been implicated in
503 ligand discrimination (Basak et al., 2020; Muroi et al., 2009; Pless & Lynch, 2009). The double mutation
504 F106L+S108C in the β2 subunit of the α4β2 nicotinic AChR subtype significantly decreases the action of
505 Ebt without altering that of ACh (Tarvin et al., 2017). In addition, loop E residues are responsible for the
506 binding energy differences α−γ versus α−δ (Nayak et al., 2016) and reduce site instability caused by
507 loop C mutations (Vij et al., 2015). Although our simulations do not shed light on these matters, the
508 temporal sequence flip-flop-fix suggests that perturbation of the loop E backbone could also play a role
509 in downstream activation of the receptor.

510 Agonists belong to efficiency classes in which $\Delta G_{LA}/\Delta G_{HA}$ is the same for all members. So far 5
511 such classes have been identified experimentally in adult-type AChRs, indicating that also are 5 pairs of
512 AC_{LA}/AC_{HA} structural classes (Indurthi & Auerbach, 2023). Although in the simulations loops C and F
513 movements, salt bridge distances were agonist dependent, with only 4 ligands we cannot associate any
514 these rearrangements with efficiency classes. Additional simulations using more agonists and with
515 binding site mutations may lead to better understanding of the dynamics that underpin molecular

516 recognition in catch and protein animation in hold, and perhaps reveal the structural basis of their
517 linkage (Auerbach, 2024).
518
519 Implications. Several aspects of this work may have general implications. The LA and HA end states of
520 hold emerged from simulations of a single protein structure and were identified by comparing
521 experimental with calculated binding energies. If general, this approach could be useful because cryo-
522 EM structures of ligands bound with LA are lacking. Agonist efficiency was calculated accurately from
523 structure alone. This, too, could be useful because efficiency allows affinity and efficacy to be
524 calculated from each other (Indurthi & Auerbach, 2021). In AChRs the up→down movement of loop C
525 flop does not impose a lid on the pocket. Rather, the up position serves to enforce catch (ligand
526 recognition) by blocking directly binding in the *trans* orientation, and the down position serves to
527 stabilize the AC_{HA} pocket and, perhaps, to deploy αY190. It is possible that the 'clamshell closures'
528 apparent in other receptors also serve to activate for reasons other than imposing a steric barrier.
529 Finally, it appears that the movement of the agonist, bound with low affinity, is the initial event in
530 gating. If confirmed, we think it both fitting and beautiful that the motion of a structural element
531 added to the system from the outside jumpstarts the allosteric transition.
532
533
534
535

536 **Materials and Methods**

537 **Hardware and Software.** All computational studies were carried out on a Linux Ubuntu 20.04 based
538 workstation with 126 GB RAM, 64 CPU cores, and two RTX A5000 24 GB GPU cards, as well as an
539 Ubuntu 20.04 based server equipped with 132 GB RAM, 96 CPU cores, and two RTX A5000 24 GB GPU
540 cards. The software utilized includes the Maestro release 2022-2 graphical user interface (GUI) of the
541 Schrödinger software suite (BioLuminate, Schrödinger, LLC, NY, USA), Amber22 (Case et al., 2005),
542 VMD 1.9.3 (Humphrey et al., 1996), ChemDraw Professional 15.1 (Purushotham et al., 2022), ChimeraX
543 (Pettersen et al., 2021), and PyMOL (PyMOL Molecular Graphics System, Version 2.0, Schrödinger, LLC).

544 **Protein preparation.** Because agonist energy changes are approximately independent of energy
545 changes in the protein outside the binding pocket, for the simulations we removed the transmembrane
546 domain and simulated only $\alpha-\delta$ subunit extracellular domain dimers. The starting structure for the
547 hold transition was resting C (PDB: 6UWZ) after toxin removal and is essentially the same as the apo
548 structure (Zarkadas et al., 2022) (Figure 1C). The 4 agonists we examined were acetylcholine (ACh),
549 carbamylcholine (CCh), epibatidine (Ebt) and epiboxidine (Ebx) (Figure 2A). These are of similar size
550 (MW 187, 183, 209 and 178, respectively) but have different efficiencies (0.50, 0.52, 0.42, and 0.46,
551 respectively) (Indurthi & Auerbach, 2023).

552 Protein preparation was conducted using the Protein Preparation Wizard (PPW) (Purushotham
553 et al., 2022) and OPLS4 force field. Bond orders were assigned to atoms based on the CCD database,
554 with zero bond orders given to bonded metals. Missing hydrogen atoms were inserted, and disulfide
555 bonds were placed appropriately. During preprocessing, structural refinement was performed with
556 Maestro's Prime utility, optimizing and adding any missing side chains and residues. Missing residues
557 were formulated by combining SEQRS information from the PDB files and optimized using Prime's

558 ePLOP module. The ionization state of all heterogeneous groups, including ligands, bound metals, and
559 charged amino acids, were determined using the EpiK tool at a pH range of 7.0 ± 2.0. Subsequent force
560 field minimization allowed for water sampling and basic restraint minimization, during which only
561 hydrogen atoms could be freely reduced.

562 The hydrogen bonding (H-bond) network underwent significant modification. The terminal chi
563 angle for residues Asn, Gln, and His was sampled through 180-degree flips, altering their spatial H-
564 bonding capabilities without affecting the fit to electron density. The neutral and protonated states of
565 His, Asp, and Glu, as well as two His tautomers, were sampled. Hydrogens on hydroxyls and thiols were
566 also analyzed to enhance the H-bond network. Finally, the ProtAssign method was employed in two
567 modes: a "regular" mode, which completed in seconds, and an "exhaustive" mode that considered
568 many more states and could take minutes or hours, depending on the H-bond network complexity.

569 **Ligand Preparation.** The two-dimensional SDF structures of carbamylcholine (CCh), acetylcholine (ACh),
570 epibatidine (Ebt) and epiboxidine (Ebx) were retrieved from the PUBCHEM database. These agonists
571 were chosen because they have a similar size and represent different efficiency classes (Indurthi &
572 Auerbach, 2023). LigPrep (LigPrep, Maestro 11.2.014, Schrödinger LLC) was utilized to construct
573 ligands, produce stereoisomers, and generate tautomers using the OPLS46 force field. Additionally, the
574 Epik module was employed to desalt and protonate the ligands at pH 7.0. Default values were applied
575 to the remaining parameters, and LigPrep was also used to prepare the ligands ACh, CCh, Ebt, and Ebx,
576 with the option "retain specified chiralities" engaged.

577 In terms of ligand state assessment, Epik can calculate a penalty to quantify the energy cost of
578 forming each state in solution based on the Hammett and Taft methods. This EpiK state penalty is
579 entirely compatible with the GlideScore used for docking, as it is computed in kcal/mol units. This

580 compatibility facilitates the examination of how the EpiK state penalty affects the GlideScore. The
581 DockingScore in Glide represents the total of the GlideScore and the Epik state penalty and served as
582 the basis for final ranking and enrichment evaluation. Furthermore, Epik offers a technique for
583 handling metal binding states, involving a change in the pH range within which the state is generated.
584 This approach underscores the comprehensive considerations made in preparing the ligands for
585 docking and subsequent analyses.

586 **Grid Generation and Molecular Docking.** The receptor grid complex of 6UWZ.pdb was generated after
587 removing alpha-bungarotoxin from the binding pocket using Glide (Glide, Maestro 11.2.014,
588 Schrödinger LLC). A virtual grid box with dimensions 20Å × 20Å × 20 Å was formed, centered within the
589 C and F loops in the α–δ binding site of the energy-minimized resting state. This grid box was used to
590 generate a receptor grid, and the default values were assigned for other parameters. Docking was
591 performed using the ligand docking wizard built into the Glide module of Schrödinger, with the default
592 scaling factor and partial charge cutoff set to 0.80 and 0.15, respectively. The docking procedure
593 consisted of two stages, extra precision (XP) followed by post-processing with prime MM-GBSA. The
594 best dock poses were selected based on dock score and MM-GBSA energy for further investigation.

595 **Molecular Dynamics Simulations.** MD simulations were conducted using the Amber22 software suite
596 within the Amber module as detailed elsewhere (Singh et al., 2021; Srivastava et al., 2022). Ligand
597 topology was prepared via the Leap module in AmberTools22, employing force field ff19SB (Tian et al.,
598 2020) and the Generalized Amber Force Field (GAFF) (Vassetti et al., 2019). The AM1BCC strategy and
599 GAFF2 were used to assign atomic charges and additional parameters. Before simulation, the systems
600 were minimized and equilibrated following a five-step minimization process, with each step involving
601 10,000 energy minimization steps. Systems were heated under NVT ensembles in two consecutive runs

602 from 0–300 K for 1 ns each, followed by a 1 ns simulation at 300 K and 1 bar pressure under the NPT
603 ensemble for equilibration. An additional 5 ns equilibration was performed before the 200 ns
604 production MD for each system, conducted under periodic boundary conditions (PBCs) and utilizing an
605 NPT ensemble with 300 K and 1 bar pressure. Long-range electrostatic interactions were treated using
606 the particle mesh Ewald method (PME), including a direct space cutoff of 12.0 Å and van der Waals
607 interactions. In production MD, a time step of 2.0 fs was employed, and the SHAKE algorithm was used
608 to keep bond lengths at equilibrium. Isobaric (NPT) conditions were maintained using the Berendsen
609 barostat, with temperature monitored by a Langevin thermostat. Coordinates from the production MD
610 were recorded in the trajectory file every 20 ps, resulting in a minimum of 10,000 frames. Trajectories
611 were analyzed using amber-tools CPPTRAJ (Roe & Cheatham, 2013), and further analysis and figure
612 generation were completed with VMD, Pymol, Xmgrace and ChimeraX. To ensure reproducibility, MD
613 trajectories were generated in triplicate.

614 **Cluster Analysis.** Cluster analysis of the ligand was performed using TCL scripts within the Visual
615 Molecular Dynamics (VMD) software, as described elsewhere (Mittal, Tonk, et al., 2021). In brief, this
616 script automates the identification of frames from the most stable conformations based on PCA
617 minima. Using these frames as input, the algorithm employed RMSD values of ligand positions to
618 cluster similar orientations. Specifically, clusters with an RMSD of ≤ 1Å were considered to share a
619 similar ligand orientation. Frames that did not fit into these top clusters were automatically excluded
620 by the script.

621 **Principal Component Analysis (PCA) and Free Energy Landscape (FEL).** PCA identifies collective
622 motions in atomic-level simulations of macromolecules (Mittal, Srivastava, et al., 2021; Srivastava et
623 al., 2022). It emphasizes significant patterns by reducing noise in MD simulations, revealing essential

624 dynamics underlying conformational changes. All equilibrated MD simulation trajectories were

625 analyzed by PCA computations using the CPPTRAJ algorithm using Amber tools.

626 Prior to PCA, least-square fitting of the protein's Cα atoms was carried out with respect to a reference

627 structure (average protein coordinates) to eliminate rotational and translational degrees of freedom in

628 the simulation box. A positional covariance matrix C (of dimensions $3N \times 3N$) was constructed using the

629 Cα atom coordinates, and this matrix was diagonalized to produce eigenvectors (directions of motion)

630 and eigenvalues (magnitudes). The elements of the covariance matrix C were obtained using:

631 $C_i = \langle (X_i - \langle X_i \rangle)(X_j - \langle X_j \rangle) \rangle$ (i, j=1,2,3…….,3N), (Eq. 1)

632 where X_i and X_j are the Cartesian coordinates of the Cα atoms, and N is the number of Cα atoms. The ⟨⟩

633 notation represents the ensemble average of atomic positions in Cartesian space. The resulting

634 principal components (eigenvectors) were sorted by the total motion they captured, generating 3N

635 eigenvectors. The free energy landscapes (FELs; Figure3) were created using the "g_sham" module in

636 GROMACS, based on the probability distribution of the top two principal components (PCs). The FEL

637 plot aids in visualizing possible conformations and corresponding energy levels. The free energy values

638 (G) were calculated as

639 $$G_i = -kT \ln(N_i/N_{max}) \quad \text{(Eq. 2)}$$

640 where k is the Boltzmann constant, T is the absolute temperature of the simulated system (300 K), N_i is

641 the population of bin i, and N_{max} is the population of the most-populated bin.

642 **Binding Free Energy Calculation.** Experimental binding free energies were estimated by using

643 electrophysiology, as described elsewhere (Indurthi & Auerbach, 2023). Briefly, the constants K_{HA} and

644 L_2 were estimated by using electrophysiology (dose-response curves, for example), and K_{HA} was

645 calculated using the thermodynamic cycle with L_0 known *a priori*. The logs of K_{LA} and K_{HA} are

646 proportional to ΔG_{LA} and ΔG_{HA}. The binding free energy of the protein-ligand docked complex (ΔG_{bind})
647 was calculated in two stages, after docking (using MM-GBSA in the Prime module of Schrödinger)
648 (Mittal, Tonk, et al., 2021; Purushotham et al., 2022) and after MD simulation on equilibrated MD
649 trajectories (using MM-PBSA/-GBSA in AMBER22). MM-PBSA is particularly useful to compare binding
650 affinities between different states and among agonists (Kollman et al., 2000; Rastelli et al., 2010; Sun et
651 al., 2014). In our use, MM-PBSA computations included both enthalpic (ΔH) contributions from
652 molecular interactions (van der Waals, electrostatics, solvation) and entropic ($T\Delta S$) contributions
653 calculated using normal mode analysis. By capturing the dynamic interplay between the ligand and
654 receptor as well as the influence of the surrounding solvent environment this approach enables
655 computation of a Gibbs free energy (ΔG).

656 After docking, for the static docked pose of the protein-ligand complex the MM-GBSA binding
657 energy calculation was performed using the OPLS4 force field and the variable-dielectric generalized
658 Born (VSGB) model in the Prime MM-GBSA module in Schrödinger 2022. We used ΔG_{bind_dock} to rank
659 protein-ligand docked complexes, selecting those with the highest negative values and dock scores as
660 the best ligands for further studies. After MD Simulation, in the MD equilibrated system binding
661 energies were calculated through the MM-PBSA/-GBSA protocol, implemented in AMBER22. This was
662 performed over the most stable clustered poses extracted from the equilibrated trajectory at minima
663 m1, m2, and m3 on the free energy landscape (FEL) over a 200 ns time frame. AMBER utilizes the
664 conventional g_mmpbsa module for MM-PBSA calculations using MM-PBSA.py script. These methods
665 calculate the energies of electrostatic interactions, van der Waals interactions, polar solvation, and
666 non-polar solvation in the equilibrated trajectory using a single trajectory protocol (STP). The binding
667 energy of each protein-ligand complex was calculated as

668 $\Delta G_{bind}=\Delta G_{complex}-\Delta G_{protein}-\Delta G_{ligand}$ where $\Delta G_{complex}$, $\Delta G_{protein}$, and ΔG_{ligand} represent the absolute free
669 energies of the complex, protein, and ligand systems, respectively. Additional terms, such as ΔH
670 (enthalpy), T and ΔS (temperature and total solute entropy), ΔG_{gas} (total gas phase energy), and ΔG_{solv}
671 (solvation energy), contribute to the calculation.

672 The Poisson-Boltzmann calculations were performed using an internal PBSA solver in Sander,
673 while Generalized Born ESURF was calculated using 'LCPO' surface areas. The vibrational mode entropy
674 contributions ($T\Delta S$) for protein-ligand interactions were calculated and averaged using normal-mode
675 analysis in Amber. The entropy term provides insights into the disorder within the system, as well as
676 how this disorder changes during the binding process. This value was added to the enthalpy term
677 computed by the MM-PBSA method to determine the absolute binding free energy (ΔG_{bind}). These
678 comprehensive calculations allowed for a precise evaluation of the interactions between the protein
679 and ligand, providing valuable insights into the binding process and its energetic characteristics.

680 **Pocket Volume Calculation.** To investigate the variations in binding site volume across all four agonist-
681 bound cases, pocket volume analysis was carried out using POVME3.0 (Wagner et al., 2017). From each
682 of the four systems, frames were extracted at consistent intervals with a stride of 2.0, culminating in
683 representative sets of 5000 protein structures for every system. Before commencing the volume
684 calculation, the trajectory was aligned, and frames were selected from VMD, serving as the initial input
685 for this method. Subsequently, an inclusion region was defined, encapsulating all binding pocket
686 conformations within the trajectory. This region's definition involved building a sphere upon which the
687 inclusion grid-points were computed, using different atoms of the ligand for this calculation.

688

689 **References:**

690 Auerbach, A. (2020). Pathways for nicotinic receptor desensitization. *J Gen Physiol*, *152*(10).
691 https://doi.org/10.1085/jgp.202012639
692 Auerbach, A. (2024). Dynamics of receptor activation by agonists [Perspective]. *Biophysical Journal*,
693 *123* (15). https://doi.org/https://doi.org/10.1016/j.bpj.2024.01.003
694 Basak, S., Kumar, A., Ramsey, S., Gibbs, E., Kapoor, A., Filizola, M., & Chakrapani, S. (2020). High-
695 resolution structures of multiple 5-HT(3A)R-setron complexes reveal a novel mechanism of
696 competitive inhibition. *Elife*, *9*. https://doi.org/10.7554/eLife.57870
697 Beene, D. L., Brandt, G. S., Zhong, W., Zacharias, N. M., Lester, H. A., & Dougherty, D. A. (2002). Cation-
698 pi interactions in ligand recognition by serotonergic (5-HT3A) and nicotinic acetylcholine
699 receptors: the anomalous binding properties of nicotine. *Biochemistry*, *41*(32), 10262-10269.
700 https://doi.org/10.1021/bi020266d
701 Bennett, W. S., Jr., & Steitz, T. A. (1978). Glucose-induced conformational change in yeast hexokinase.
702 *Proc Natl Acad Sci U S A*, *75*(10), 4848-4852. https://doi.org/10.1073/pnas.75.10.4848
703 Blum, A. P., Lester, H. A., & Dougherty, D. A. (2010). Nicotinic pharmacophore: the pyridine N of
704 nicotine and carbonyl of acetylcholine hydrogen bond across a subunit interface to a backbone
705 NH. *Proc Natl Acad Sci U S A*, *107*(30), 13206-13211. https://doi.org/10.1073/pnas.1007140107
706 Brown, F. K., & Kollman, P. A. (1987). Molecular dynamics simulations of "loop closing" in the enzyme
707 triose phosphate isomerase. *J Mol Biol*, *198*(3), 533-546. https://doi.org/10.1016/0022-
708 2836(87)90298-1
709 Bruhova, I., & Auerbach, A. (2017). Molecular recognition at cholinergic synapses: acetylcholine versus
710 choline. *J Physiol*, *595*(4), 1253-1261. https://doi.org/10.1113/JP273291
711 Case, D. A., Cheatham, T. E., 3rd, Darden, T., Gohlke, H., Luo, R., Merz, K. M., Jr., Onufriev, A.,
712 Simmerling, C., Wang, B., & Woods, R. J. (2005). The Amber biomolecular simulation programs.
713 *J Comput Chem*, *26*(16), 1668-1688. https://doi.org/10.1002/jcc.20290
714 Celie, P. H., van Rossum-Fikkert, S. E., van Dijk, W. J., Brejc, K., Smit, A. B., & Sixma, T. K. (2004).
715 Nicotine and carbamylcholine binding to nicotinic acetylcholine receptors as studied in AChBP
716 crystal structures. *Neuron*, *41*(6), 907-914. https://doi.org/10.1016/s0896-6273(04)00115-1
717 Chang, Y., & Weiss, D. S. (2002). Site-specific fluorescence reveals distinct structural changes with
718 GABA receptor activation and antagonism. *Nat Neurosci*, *5*(11), 1163-1168.
719 https://doi.org/10.1038/nn926
720 Chen, S., Zhao, Y., Wang, Y., Shekhar, M., Tajkhorshid, E., & Gouaux, E. (2017). Activation and
721 Desensitization Mechanism of AMPA Receptor-TARP Complex by Cryo-EM. *Cell*, *170*(6), 1234-
722 1246 e1214. https://doi.org/10.1016/j.cell.2017.07.045
723 Du, J., Lu, W., Wu, S., Cheng, Y., & Gouaux, E. (2015). Glycine receptor mechanism elucidated by
724 electron cryo-microscopy. *Nature*, *526*(7572), 224-229. https://doi.org/10.1038/nature14853
725 Furukawa, H., Singh, S. K., Mancusso, R., & Gouaux, E. (2005). Subunit arrangement and function in
726 NMDA receptors. *Nature*, *438*(7065), 185-192. https://doi.org/10.1038/nature04089
727 Gay, E. A., & Yakel, J. L. (2007). Gating of nicotinic ACh receptors; new insights into structural
728 transitions triggered by agonist binding that induce channel opening. *J Physiol*, *584*(Pt 3), 727-
729 733. https://doi.org/10.1113/jphysiol.2007.142554

730 Genheden, S., & Ryde, U. (2015). The MM/PBSA and MM/GBSA methods to estimate ligand-binding
731 affinities. *Expert Opin Drug Discov*, *10*(5), 449-461.
732 https://doi.org/10.1517/17460441.2015.1032936
733 Grosman, C., & Auerbach, A. (2001). The dissociation of acetylcholine from open nicotinic receptor
734 channels. *Proc Natl Acad Sci U S A*, *98*(24), 14102-14107.
735 https://doi.org/10.1073/pnas.251402498
736 Grosman, C., Zhou, M., & Auerbach, A. (2000). Mapping the conformational wave of acetylcholine
737 receptor channel gating. *Nature*, *403*(6771), 773-776. https://doi.org/10.1038/35001586
738 Gupta, S., Chakraborty, S., Vij, R., & Auerbach, A. (2017). A mechanism for acetylcholine receptor
739 gating based on structure, coupling, phi, and flip. *J Gen Physiol*, *149*(1), 85-103.
740 https://doi.org/10.1085/jgp.201611673
741 Hansen, S. B., Sulzenbacher, G., Huxford, T., Marchot, P., Taylor, P., & Bourne, Y. (2005). Structures of
742 Aplysia AChBP complexes with nicotinic agonists and antagonists reveal distinctive binding
743 interfaces and conformations. *Embo Journal*, *24*(20), 3635-3646.
744 https://doi.org/10.1038/sj.emboj.7600828
745 Hibbs, R. E., & Gouaux, E. (2011). Principles of activation and permeation in an anion-selective Cys-loop
746 receptor. *Nature*, *474*(7349), 54-60. https://doi.org/10.1038/nature10139
747 Hibbs, R. E., Sulzenbacher, G., Shi, J., Talley, T. T., Conrod, S., Kem, W. R., Taylor, P., Marchot, P., &
748 Bourne, Y. (2009). Structural determinants for interaction of partial agonists with acetylcholine
749 binding protein and neuronal alpha7 nicotinic acetylcholine receptor. *Embo Journal*, *28*(19),
750 3040-3051. https://doi.org/10.1038/emboj.2009.227
751 Hou, T., Wang, J., Li, Y., & Wang, W. (2011). Assessing the performance of the MM/PBSA and
752 MM/GBSA methods. 1. The accuracy of binding free energy calculations based on molecular
753 dynamics simulations. *Journal of Chemical Information and Modeling*, *51*(1), 69-82.
754 https://doi.org/10.1021/ci100275a
755 Huang, W., Manglik, A., Venkatakrishnan, A. J., Laeremans, T., Feinberg, E. N., Sanborn, A. L., Kato, H.
756 E., Livingston, K. E., Thorsen, T. S., Kling, R. C., Granier, S., Gmeiner, P., Husbands, S. M.,
757 Traynor, J. R., Weis, W. I., Steyaert, J., Dror, R. O., & Kobilka, B. K. (2015). Structural insights into
758 micro-opioid receptor activation. *Nature*, *524*(7565), 315-321.
759 https://doi.org/10.1038/nature14886
760 Humphrey, W., Dalke, A., & Schulten, K. (1996). VMD: visual molecular dynamics. *J Mol Graph*, *14*(1),
761 33-38, 27-38. https://doi.org/10.1016/0263-7855(96)00018-5
762 Indurthi, D., & Auerbach, A. (2021). Agonist Efficiency Estimated from Concentration Response Curve.
763 *Biophysical Journal*, *120*(3), 57a-57a. <Go to ISI>://WOS:000629601400276
764 Indurthi, D. C., & Auerbach, A. (2023). Agonist efficiency links binding and gating in a nicotinic receptor.
765 *Elife*, *12*. https://doi.org/10.7554/eLife.86496
766 Jackson, M. B. (1986). Kinetics of unliganded acetylcholine receptor channel gating. *Biophys J*, *49*(3),
767 663-672. https://doi.org/10.1016/S0006-3495(86)83693-1
768 Jadey, S., & Auerbach, A. (2012). An integrated catch-and-hold mechanism activates nicotinic
769 acetylcholine receptors. *J Gen Physiol*, *140*(1), 17-28. https://doi.org/10.1085/jgp.201210801
770 Jones, M. V., Jonas, P., Sahara, Y., & Westbrook, G. L. (2001). Microscopic kinetics and energetics
771 distinguish GABA(A) receptor agonists from antagonists. *Biophys J*, *81*(5), 2660-2670.
772 https://doi.org/10.1016/S0006-3495(01)75909-7

773 Klabunde, T., Petrassi, H. M., Oza, V. B., Raman, P., Kelly, J. W., & Sacchettini, J. C. (2000). Rational
774 design of potent human transthyretin amyloid disease inhibitors. *Nat Struct Biol*, *7*(4), 312-321.
775 https://doi.org/10.1038/74082
776 Klei, H. E., Kish, K., Lin, P. F., Guo, Q., Friborg, J., Rose, R. E., Zhang, Y., Goldfarb, V., Langley, D. R.,
777 Wittekind, M., & Sheriff, S. (2007). X-ray crystal structures of human immunodeficiency virus
778 type 1 protease mutants complexed with atazanavir. *J Virol*, *81*(17), 9525-9535.
779 https://doi.org/10.1128/JVI.02503-05
780 Kollman, P. A., Massova, I., Reyes, C., Kuhn, B., Huo, S., Chong, L., Lee, M., Lee, T., Duan, Y., Wang, W.,
781 Donini, O., Cieplak, P., Srinivasan, J., Case, D. A., & Cheatham, T. E., 3rd. (2000). Calculating
782 structures and free energies of complex molecules: combining molecular mechanics and
783 continuum models. *Acc Chem Res*, *33*(12), 889-897. https://doi.org/10.1021/ar000033j
784 Ma, W., Tang, C., & Lai, L. (2005). Specificity of trypsin and chymotrypsin: loop-motion-controlled
785 dynamic correlation as a determinant. *Biophys J*, *89*(2), 1183-1193.
786 https://doi.org/10.1529/biophysj.104.057158
787 Mittal, L., Srivastava, M., Kumari, A., Tonk, R. K., Awasthi, A., & Asthana, S. (2021). Interplay among
788 Structural Stability, Plasticity, and Energetics Determined by Conformational Attuning of
789 Flexible Loops in PD-1. *Journal of Chemical Information and Modeling*, *61*(1), 358-384.
790 https://doi.org/10.1021/acs.jcim.0c01080
791 Mittal, L., Tonk, R. K., Awasthi, A., & Asthana, S. (2021). Targeting cryptic-orthosteric site of PD-L1 for
792 inhibitor identification using structure-guided approach. *Arch Biochem Biophys*, *713*, 109059.
793 https://doi.org/10.1016/j.abb.2021.109059
794 Mortensen, M., Ebert, B., Wafford, K., & Smart, T. G. (2010). Distinct activities of GABA agonists at
795 synaptic- and extrasynaptic-type GABAA receptors. *J Physiol*, *588*(Pt 8), 1251-1268.
796 https://doi.org/10.1113/jphysiol.2009.182444
797 Mukhtasimova, N., Free, C., & Sine, S. M. (2005). Initial coupling of binding to gating mediated by
798 conserved residues in the muscle nicotinic receptor. *J Gen Physiol*, *126*(1), 23-39.
799 https://doi.org/10.1085/jgp.200509283
800 Munro, L., Ladefoged, L. K., Padmanathan, V., Andersen, S., Schiott, B., & Kristensen, A. S. (2019).
801 Conformational Changes in the 5-HT(3A) Receptor Extracellular Domain Measured by Voltage-
802 Clamp Fluorometry. *Molecular Pharmacology*, *96*(6), 720-734.
803 https://doi.org/10.1124/mol.119.116657
804 Muroi, Y., Theusch, C. M., Czajkowski, C., & Jackson, M. B. (2009). Distinct structural changes in the
805 GABAA receptor elicited by pentobarbital and GABA. *Biophys J*, *96*(2), 499-509.
806 https://doi.org/10.1016/j.bpj.2008.09.037
807 Nayak, T. K., & Auerbach, A. (2013). Asymmetric transmitter binding sites of fetal muscle acetylcholine
808 receptors shape their synaptic response. *Proc Natl Acad Sci U S A*, *110*(33), 13654-13659.
809 https://doi.org/10.1073/pnas.1308247110
810 Nayak, T. K., & Auerbach, A. (2017). Cyclic activation of endplate acetylcholine receptors. *Proc Natl*
811 *Acad Sci U S A*, *114*(45), 11914-11919. https://doi.org/10.1073/pnas.1711228114
812 Nayak, T. K., Chakraborty, S., Zheng, W. J., & Auerbach, A. (2016). Structural correlates of affinity in
813 fetal versus adult endplate nicotinic receptors. *Nature Communications*, *7*.
814 https://doi.org/ARTN 11352
815 10.1038/ncomms11352

816 Nayak, T. K., Purohit, P. G., & Auerbach, A. (2012). The intrinsic energy of the gating isomerization of a
817 neuromuscular acetylcholine receptor channel. *J Gen Physiol*, *139*(5), 349-358.
818 https://doi.org/10.1085/jgp.201110752
819 Nayak, T. K., Vij, R., Bruhova, I., Shandilya, J., & Auerbach, A. (2019). Efficiency measures the
820 conversion of agonist binding energy into receptor conformational change. *J Gen Physiol*,
821 *151*(4), 465-477. https://doi.org/10.1085/jgp.201812215
822 Nickbarg, E. B., Davenport, R. C., Petsko, G. A., & Knowles, J. R. (1988). Triosephosphate isomerase:
823 removal of a putatively electrophilic histidine residue results in a subtle change in catalytic
824 mechanism. *Biochemistry*, *27*(16), 5948-5960. https://doi.org/10.1021/bi00416a019
825 Noviello, C. M., Gharpure, A., Mukhtasimova, N., Cabuco, R., Baxter, L., Borek, D., Sine, S. M., & Hibbs,
826 R. E. (2021). Structure and gating mechanism of the alpha7 nicotinic acetylcholine receptor.
827 *Cell*, *184*(8), 2121-2134 e2113. https://doi.org/10.1016/j.cell.2021.02.049
828 Oostenbrink, C., Villa, A., Mark, A. E., & van Gunsteren, W. F. (2004). A biomolecular force field based
829 on the free enthalpy of hydration and solvation: the GROMOS force-field parameter sets 53A5
830 and 53A6. *J Comput Chem*, *25*(13), 1656-1676. https://doi.org/10.1002/jcc.20090
831 Padgett, C. L., Hanek, A. P., Lester, H. A., Dougherty, D. A., & Lummis, S. C. (2007). Unnatural amino
832 acid mutagenesis of the GABA(A) receptor binding site residues reveals a novel cation-pi
833 interaction between GABA and beta 2Tyr97. *Journal of Neuroscience*, *27*(4), 886-892.
834 https://doi.org/10.1523/JNEUROSCI.4791-06.2007
835 Pettersen, E. F., Goddard, T. D., Huang, C. C., Meng, E. C., Couch, G. S., Croll, T. I., Morris, J. H., & Ferrin,
836 T. E. (2021). UCSF ChimeraX: Structure visualization for researchers, educators, and developers.
837 *Protein Sci*, *30*(1), 70-82. https://doi.org/10.1002/pro.3943
838 Phillips, R. (2020). *The Molecular Switch: Signaling and Allostery*. Prinston University Press.
839 Plapp, B. V. (2010). Conformational changes and catalysis by alcohol dehydrogenase. *Arch Biochem*
840 *Biophys*, *493*(1), 3-12. https://doi.org/10.1016/j.abb.2009.07.001
841 Pless, S. A., Hanek, A. P., Price, K. L., Lynch, J. W., Lester, H. A., Dougherty, D. A., & Lummis, S. C. (2011).
842 A cation-pi interaction at a phenylalanine residue in the glycine receptor binding site is
843 conserved for different agonists. *Molecular Pharmacology*, *79*(4), 742-748.
844 https://doi.org/10.1124/mol.110.069583
845 Pless, S. A., & Lynch, J. W. (2009). Ligand-specific conformational changes in the alpha1 glycine
846 receptor ligand-binding domain. *J Biol Chem*, *284*(23), 15847-15856.
847 https://doi.org/10.1074/jbc.M809343200
848 Polovinkin, L., Hassaine, G., Perot, J., Neumann, E., Jensen, A. A., Lefebvre, S. N., Corringer, P. J.,
849 Neyton, J., Chipot, C., Dehez, F., Schoehn, G., & Nury, H. (2018). Conformational transitions of
850 the serotonin 5-HT(3) receptor. *Nature*, *563*(7730), 275-279. https://doi.org/10.1038/s41586-
851 018-0672-3
852 Purohit, P., & Auerbach, A. (2009). Unliganded gating of acetylcholine receptor channels. *Proc Natl*
853 *Acad Sci U S A*, *106*(1), 115-120. https://doi.org/10.1073/pnas.0809272106
854 Purohit, P., & Auerbach, A. (2013). Loop C and the mechanism of acetylcholine receptor-channel
855 gating. *J Gen Physiol*, *141*(4), 467-478. https://doi.org/10.1085/jgp.201210946
856 Purohit, P., Bruhova, I., Gupta, S., & Auerbach, A. (2014). Catch-and-Hold Activation of Muscle
857 Acetylcholine Receptors Having Transmitter Binding Site Mutations. *Biophysical Journal*, *107*(1),
858 88-99. https://doi.org/10.1016/j.bpj.2014.04.057

859 Purohit, P., Gupta, S., Jadey, S., & Auerbach, A. (2013). Functional anatomy of an allosteric protein.
860 *Nature Communications*, *4*, 2984. https://doi.org/10.1038/ncomms3984
861 Purushotham, N., Singh, M., Paramesha, B., Kumar, V., Wakode, S., Banerjee, S. K., Poojary, B., &
862 Asthana, S. (2022). Design and synthesis of amino acid derivatives of substituted
863 benzimidazoles and pyrazoles as Sirt1 inhibitors. *RSC Adv*, *12*(7), 3809-3827.
864 https://doi.org/10.1039/d1ra06149f
865 Rahman, M. M., Basta, T., Teng, J., Lee, M., Worrell, B. T., Stowell, M. H. B., & Hibbs, R. E. (2022).
866 Structural mechanism of muscle nicotinic receptor desensitization and block by curare. *Nat*
867 *Struct Mol Biol*, *29*(4), 386-394. https://doi.org/10.1038/s41594-022-00737-3
868 Rahman, M. M., Teng, J., Worrell, B. T., Noviello, C. M., Lee, M., Karlin, A., Stowell, M. H. B., & Hibbs, R.
869 E. (2020). Structure of the Native Muscle-type Nicotinic Receptor and Inhibition by Snake
870 Venom Toxins. *Neuron*, *106*(6), 952-962 e955. https://doi.org/10.1016/j.neuron.2020.03.012
871 Rasmussen, S. G., DeVree, B. T., Zou, Y., Kruse, A. C., Chung, K. Y., Kobilka, T. S., Thian, F. S., Chae, P. S.,
872 Pardon, E., Calinski, D., Mathiesen, J. M., Shah, S. T., Lyons, J. A., Caffrey, M., Gellman, S. H.,
873 Steyaert, J., Skiniotis, G., Weis, W. I., Sunahara, R. K., & Kobilka, B. K. (2011). Crystal structure of
874 the beta2 adrenergic receptor-Gs protein complex. *Nature*, *477*(7366), 549-555.
875 https://doi.org/10.1038/nature10361
876 Rastelli, G., Del Rio, A., Degliesposti, G., & Sgobba, M. (2010). Fast and accurate predictions of binding
877 free energies using MM-PBSA and MM-GBSA. *J Comput Chem*, *31*(4), 797-810.
878 https://doi.org/10.1002/jcc.21372
879 Richard, J. P. (2022). Enabling Role of Ligand-Driven Conformational Changes in Enzyme Evolution.
880 *Biochemistry*, *61*(15), 1533-1542. https://doi.org/10.1021/acs.biochem.2c00178
881 Roe, D. R., & Cheatham, T. E., 3rd. (2013). PTRAJ and CPPTRAJ: Software for Processing and Analysis of
882 Molecular Dynamics Trajectory Data. *J Chem Theory Comput*, *9*(7), 3084-3095.
883 https://doi.org/10.1021/ct400341p
884 Sauguet, L., Shahsavar, A., Poitevin, F., Huon, C., Menny, A., Nemecz, A., Haouz, A., Changeux, J. P.,
885 Corringer, P. J., & Delarue, M. (2014). Crystal structures of a pentameric ligand-gated ion
886 channel provide a mechanism for activation. *Proc Natl Acad Sci U S A*, *111*(3), 966-971.
887 https://doi.org/10.1073/pnas.1314997111
888 Shang, Y., Yeatman, H. R., Provasi, D., Alt, A., Christopoulos, A., Canals, M., & Filizola, M. (2016).
889 Proposed Mode of Binding and Action of Positive Allosteric Modulators at Opioid Receptors.
890 *ACS Chem Biol*, *11*(5), 1220-1229. https://doi.org/10.1021/acschembio.5b00712
891 Sigel, E., & Steinmann, M. E. (2012). Structure, function, and modulation of GABA(A) receptors. *J Biol*
892 *Chem*, *287*(48), 40224-40231. https://doi.org/10.1074/jbc.R112.386664
893 Singh, M., Srivastava, M., Wakode, S. R., & Asthana, S. (2021). Elucidation of Structural Determinants
894 Delineates the Residues Playing Key Roles in Differential Dynamics and Selective Inhibition of
895 Sirt1-3. *Journal of Chemical Information and Modeling*, *61*(3), 1105-1124.
896 https://doi.org/10.1021/acs.jcim.0c01193
897 Srivastava, M., Mittal, L., Kumari, A., Agrahari, A. K., Singh, M., Mathur, R., & Asthana, S. (2022).
898 Characterizing (un)binding mechanism of USP7 inhibitors to unravel the cause of enhanced
899 binding potencies at allosteric checkpoint. *Protein Sci*, *31*(9), e4398.
900 https://doi.org/10.1002/pro.4398
901 Sun, H., Li, Y., Tian, S., Xu, L., & Hou, T. (2014). Assessing the performance of MM/PBSA and MM/GBSA
902 methods. 4. Accuracies of MM/PBSA and MM/GBSA methodologies evaluated by various

903 simulation protocols using PDBbind data set. *Phys Chem Chem Phys*, *16*(31), 16719-16729.
904 https://doi.org/10.1039/c4cp01388c
905 Taly, A., Corringer, P. J., Guedin, D., Lestage, P., & Changeux, J. P. (2009). Nicotinic receptors: allosteric
906 transitions and therapeutic targets in the nervous system. *Nature Reviews Drug Discovery*, *8*(9),
907 733-750. https://doi.org/10.1038/nrd2927
908 Tarvin, R. D., Borghese, C. M., Sachs, W., Santos, J. C., Lu, Y., O'Connell, L. A., Cannatella, D. C., Harris, R.
909 A., & Zakon, H. H. (2017). Interacting amino acid replacements allow poison frogs to evolve
910 epibatidine resistance. *Science*, *357*(6357), 1261-1266.
911 https://doi.org/10.1126/science.aan5061
912 Tian, C., Kasavajhala, K., Belfon, K. A. A., Raguette, L., Huang, H., Migues, A. N., Bickel, J., Wang, Y.,
913 Pincay, J., Wu, Q., & Simmerling, C. (2020). ff19SB: Amino-Acid-Specific Protein Backbone
914 Parameters Trained against Quantum Mechanics Energy Surfaces in Solution. *J Chem Theory*
915 *Comput*, *16*(1), 528-552. https://doi.org/10.1021/acs.jctc.9b00591
916 Tripathy, S., Zheng, W., & Auerbach, A. (2019). A single molecular distance predicts agonist binding
917 energy in nicotinic receptors. *J Gen Physiol*, *151*(4), 452-464.
918 https://doi.org/10.1085/jgp.201812212
919 Unwin, N. (1993). Nicotinic acetylcholine receptor at 9 A resolution. *J Mol Biol*, *229*(4), 1101-1124.
920 https://doi.org/10.1006/jmbi.1993.1107
921 Vassetti, D., Pagliai, M., & Procacci, P. (2019). Assessment of GAFF2 and OPLS-AA General Force Fields
922 in Combination with the Water Models TIP3P, SPCE, and OPC3 for the Solvation Free Energy of
923 Druglike Organic Molecules. *J Chem Theory Comput*, *15*(3), 1983-1995.
924 https://doi.org/10.1021/acs.jctc.8b01039
925 Vij, R., Purohit, P., & Auerbach, A. (2015). Modal affinities of endplate acetylcholine receptors caused
926 by loop C mutations. *J Gen Physiol*, *146*(5), 375-386. https://doi.org/10.1085/jgp.201511503
927 Wagner, J. R., Sorensen, J., Hensley, N., Wong, C., Zhu, C., Perison, T., & Amaro, R. E. (2017). POVME
928 3.0: Software for Mapping Binding Pocket Flexibility. *J Chem Theory Comput*, *13*(9), 4584-4592.
929 https://doi.org/10.1021/acs.jctc.7b00500
930 Walsh, R. M., Jr., Roh, S. H., Gharpure, A., Morales-Perez, C. L., Teng, J., & Hibbs, R. E. (2018). Structural
931 principles of distinct assemblies of the human alpha4beta2 nicotinic receptor. *Nature*,
932 *557*(7704), 261-265. https://doi.org/10.1038/s41586-018-0081-7
933 Wlodawer, A., & Erickson, J. W. (1993). Structure-based inhibitors of HIV-1 protease. *Annu Rev*
934 *Biochem*, *62*, 543-585. https://doi.org/10.1146/annurev.bi.62.070193.002551
935 Xiu, X., Puskar, N. L., Shanata, J. A., Lester, H. A., & Dougherty, D. A. (2009). Nicotine binding to brain
936 receptors requires a strong cation-pi interaction. *Nature*, *458*(7237), 534-537.
937 https://doi.org/10.1038/nature07768
938 Yu, A., Salazar, H., Plested, A. J. R., & Lau, A. Y. (2018). Neurotransmitter Funneling Optimizes
939 Glutamate Receptor Kinetics. *Neuron*, *97*(1), 139-149 e134.
940 https://doi.org/10.1016/j.neuron.2017.11.024
941 Yu, R., Hurdiss, E., Greiner, T., Lape, R., Sivilotti, L., & Biggin, P. C. (2014). Agonist and antagonist
942 binding in human glycine receptors. *Biochemistry*, *53*(38), 6041-6051.
943 https://doi.org/10.1021/bi500815f
944 Zarkadas, E., Pebay-Peyroula, E., Thompson, M. J., Schoehn, G., Uchanski, T., Steyaert, J., Chipot, C.,
945 Dehez, F., Baenziger, J. E., & Nury, H. (2022). Conformational transitions and ligand-binding to a

946 muscle-type nicotinic acetylcholine receptor. *Neuron*, *110*(8), 1358-1370 e1355.
947 https://doi.org/10.1016/j.neuron.2022.01.013
948 Zhong, W., Gallivan, J. P., Zhang, Y., Li, L., Lester, H. A., & Dougherty, D. A. (1998). From ab initio
949 quantum mechanics to molecular neurobiology: a cation-pi binding site in the nicotinic
950 receptor. *Proc Natl Acad Sci U S A*, *95*(21), 12088-12093.
951 https://doi.org/10.1073/pnas.95.21.12088
952